

**UNIVERSITY OF THE WESTERN CAPE**

# **Coulomb Excitation of $^{66}\text{Ge}$**

by

**Kenzo Abrahams**

A thesis submitted in conformity with the requirements for the  
degree of Doctor of Philosophy

in the  
**Faculty of Science**  
**Department of Physics**

Supervisor: Nico Orce

January 2021

# **Declaration**

I, Kenzo Abrahams, declare that this thesis “Coulomb Excitation of  $^{66}\text{Ge}$ ” is my own work, that it has not been submitted before for any degree or assessment at any other university, and that all the sources I have used or quoted have been indicated and acknowledged by means of complete references.

Signature:.....

Date:.....

*“The most exciting phrase to hear in science, the one that heralds the most discoveries, is not ‘Eureka!’ but ‘That’s funny...’”*

Isaac Asimov

# **Abstract**

The SASL project at the University of the Western Cape is in the process of developing a machine translation system that can translate fully-fledged phrases between South African Sign Language (SASL) and English in real-time. To visualise sign language, the system aims to make use of a 3D humanoid avatar created by van Wyk. Moemedi used this avatar to create an animation system that visualises a small set of simple phrases from very simple SignWriting notation input. This research aims to achieve an animation system that can render full sign language sentences given complex SignWriting notation glyphs with multiple sections. The specific focus of the research is achieving animations that are accurate representations of the SignWriting input in terms of the five fundamental parameters of sign language, namely, hand motion, location, orientation and shape, as well as non-manual features such as facial expressions. An experiment was carried out to determine the accuracy of the proposed system on a set of 20 SASL phrases annotated with SignWriting notation. It was found that the proposed system is highly accurate, achieving an average accuracy of 81.6%.

# **Keywords**

Animation, Humanoid avatar, SignWriting, Key frame animation, Blender.

# Acknowledgements

First and foremost, I would thank God for giving me the strength, health and wisdom to do my masters at the University of the Western Cape. It is truly a blessing to be able to wake up on a daily basis and pursue my dreams.

I would also like to thank my parents for giving me the opportunity to further my education. I am truly indebted to them. They have taught me the value of life and supported me 120% all the way. I am grateful that they have bestowed upon me the knowledge and wisdom to make the correct choices in life. Without their support, I could not have reached this milestone in my life.

I would especially like to thank my supervisor Mr Mehrdad Ghaziasgar for his outstanding guidance, inspiration and encouragement. Thank you for your patience with me and for availing yourself whenever I needed assistance; your open door policy was much appreciated. Your guidance during the course of my masters degree was invaluable. I would also like to thank Mr James Connan for his guidance from afar. Being able to call you when I had a problem or needed guidance was invaluable to my research.

I would like to thank Imran Achmed and Dane Brown for their generous advice and assistance during the first half of my masters. It is highly appreciated. I would also like to thank my lab mates, Roland Foster and Nathan De La Cruz, for creating an environment which was easy to work in.

I would like to thank the University of the Western Cape for the opportunity to study here. I thank my lecturers for educating me and helping me acquire knowledge in the field of computer science, physics and other fields in life. I would especially like to thank Mr Dodds for his guidance with latex and opening my eyes to a different paradigm of computer science through the course known as compilers. It was definitely the most interesting course I have encountered throughout the course of my studies and has aligned my thinking with the unique ability to solve problems by thinking outside of the box.

Last but definitely not least, I would like to thank my best friend and girlfriend Charlize Dankers for always motivating and supporting me all the way during my masters and even before then. I appreciate your attempts to make me feel better when the work load was applying pressure and stressing me out. I am truly thankful.

# Contents

<b>Declaration of Authorship</b>	i
<b>Abstract</b>	iii
<b>Keywords</b>	iii
<b>Acknowledgements</b>	iv
<b>List of Figures</b>	vii
<b>List of Tables</b>	x
<b>Abbreviations</b>	xi
<b>1 Introduction</b>	1
1.1 Scientific motivation . . . . .	3
<b>2 Coulomb Excitation Theory</b>	6
2.1 Theory Description . . . . .	7
2.1.1 Semiclassical approximation . . . . .	8
2.1.2 First-order Perturbation Theory . . . . .	10
2.1.3 Second-order Perturbation Theory . . . . .	13
2.2 Gosia . . . . .	14
<b>3 Experimental Methodology</b>	17
3.1 ISOLDE facility . . . . .	17
3.1.1 Isotope Production . . . . .	17
3.1.1.1 GPS . . . . .	20
3.1.2 Post-acceleration . . . . .	20
3.1.2.1 REXTRAP . . . . .	21
3.1.2.2 REXEBIS . . . . .	21
3.1.2.3 A/q separator . . . . .	22
3.1.2.4 REXLINAC . . . . .	23
3.1.2.5 HIELINAC . . . . .	23

3.1.3	Beam Time Structure . . . . .	24
3.2	MINIBALL . . . . .	26
3.2.1	High-Purity Germanium Detectors . . . . .	27
3.2.2	Particle Detector . . . . .	28
3.2.3	Data Acquisition . . . . .	29
<b>4</b>	<b>Data Analysis and Results</b>	<b>31</b>
4.1	Detector Calibration . . . . .	31
4.1.1	HPGe Cluster Calibration . . . . .	31
4.1.2	DSSSD Energy Calibration . . . . .	33
4.2	Doppler Correction . . . . .	34
4.3	Particle- $\gamma$ Coincidence . . . . .	37
4.4	Beam Composition . . . . .	38
4.4.1	$\beta$ -decay investigation . . . . .	41
4.5	Extracting Nuclear Structure Information . . . . .	45
4.5.1	Determination of $B(E2)$ . . . . .	48
4.5.2	Determination of $Q_s$ . . . . .	50
<b>5</b>	<b>Results and Discussion</b>	<b>53</b>
<b>6</b>	<b>Conclusion</b>	<b>56</b>
<b>A</b>	<b>Additional Test Results 1</b>	<b>57</b>
<b>B</b>	<b>Additional Test Results 2</b>	<b>58</b>
<b>Bibliography</b>		<b>59</b>

# List of Figures

1.1	The $2_1^+$ energy levels in keV for even-even Germanium isotopes from $^{64}\text{Ge}$ to $^{76}\text{Ge}$ (Top). $B(E2; 2_1^+ \rightarrow 0_1^+)$ values for the same range of even-even Germanium nuclei. . . . .	3
1.2	Comparison of rotational parameter for Sr, Kr, Se isotopes and $^{66}\text{Ge}$ showing a similar trend. . . . .	4
2.1	Nuclear shapes based on the value of the spectroscopic quadrupole moment $Q_s$ . . . . .	7
2.2	A CE scattering event in the LAB frame. At the point of closest approach $b$ , the interaction potential is the strongest. The hypobolic path which the projectile follows is illustrated by the blue arrow. . . . .	7
2.3	A one-step excitation from an intial state $ i\rangle$ to a final state $ f\rangle$ , with the excitation and deexcitation clearly shown. In this case, a E2 transition in a even-even nuclei is observed. . . . .	11
2.4	Schematic representation of the reorientation effect. The final state $ f\rangle$ can be reached via an intermediate state $ m\rangle$ . The final state can be one of the magnetic substates of the excited state. The splitting of the energy levels that the magnetic substates can take on is dependant on the static quadrupole moment by the relation $E(t) \sim eQ_s Z/r^3(t)$ . . . . .	14
3.1	Schematic overview of the ISOLDE facility after the HIE-ISOLDE upgrades. There are many experimental setups in the ISOLDE hall, only those during this experiment have been labelled. . . . .	18
3.2	Schematic overview of the beam line layout in the ISOLDE hall. Both the HRS and GPS mass seperators are illustrated [29]. . . . .	19
3.3	The GPS switchyard [29]. . . . .	20
3.4	A detailed layout of REX-ISOLDE. [23]. . . . .	21
3.5	Images of REXTRAP (left) and REXEBIS (right) at ISOLDE, CERN. . .	22
3.6	REXLINAC at ISOLDE, CERN. A breakdown of the components that make up the LINAC are shown. [21] . . . . .	23
3.7	One of the cryomodules being installed in the ISOLDE hall. [7] . . . .	24
3.8	Time structure for the radioactive ion beam at CERN. See text for more details. . . . .	25
3.9	The target chamber used in the CE of $^{66}\text{Ge}$ surrounded by the triple cluster germainium detectors. Figure adapted from [37]. . . . .	26
3.10	Four triple clusters mounted on the one half of the MINIBALL frame. The four degrees of freedom are marked. Figure adapted from [37]. . . .	27

3.11	Left: A single MINIBALL triple cluster connect to the liquid nitrogen dewar for cooling purposes. Right: Exploded view of one of the segmented germanium crystals. . . . .	28
3.12	Schematic drawing of the double-sided strip detector. The front side has 0.1 mm, inactive regions between the rings and the back side consists of 0.1° inactive regions between the strips. . . . .	29
3.13	Picture of the DSSSD mounted in the target chamber. The 16 annular rings can be seen [37]. . . . .	29
3.14	Schematic illustration of the data processing of MARABOU. [32]. . . . .	30
4.1	A spectrum of the $^{152}\text{Eu}$ and $^{133}\text{Ba}$ calibration sources used to calibrate the clover detectors. Peaks with red labels belong to $^{133}\text{Ba}$ and the those with black labels belong to $^{152}\text{Eu}$ . . . . .	32
4.2	A fit to the $^{152}\text{Eu}$ data for one of the core of a clover detector. The gain and offset are given in the equation of the linear fit. . . . .	33
4.3	The kinematics obtained with LISE++ for $^{16}\text{O}$ onto $^{196}\text{Pt}$ as a function of scattering angle. The dashed lines represents the angles that the different rings cover in the lab frame. . . . .	34
4.4	The kinematics obtained with LISE++ for $^{16}\text{O}$ onto $^{196}\text{Pt}$ as a function of scattering angle. The dashed line represents the angles that the different rings cover in the lab frame. . . . .	35
4.5	The kinematics obtained with LISE++ for $^{16}\text{O}$ onto $^{196}\text{Pt}$ as a function of scattering angle. The dashed line represents the angles that the different rings cover in the lab frame. . . . .	35
4.6	The parameters used to calibrate the position of each triple cluster with respect to the beam line. . . . .	37
4.7	A $\gamma$ -ray singles spectrum for $^{66}\text{Ge}$ on $^{196}\text{Pt}$ with no particle- $\gamma$ coincidence conditions applied. The energy of the first $2^+$ transition at 956 keV is marked. . . . .	38
4.8	Time difference between the clover detectors and the DSSSD. Prompt and random time windows are marked, which are used to generate the final $\gamma$ -ray spectra. . . . .	39
4.9	The resulting $\gamma$ -ray spectrum from the prompt time window. The range of this spectrum was decreased to not include the 511 keV transition such that the first $2^+$ state in $^{66}\text{Ge}$ can be seen. . . . .	39
4.10	The resulting beam gated $\gamma$ -ray spectrum after background subtraction. The first $2^+$ state in $^{196}\text{Pt}$ is marked. . . . .	40
4.11	The resulting $\gamma$ -ray spectrum after Doppler correction and background subtraction. The first $2^+$ state in $^{66}\text{Ge}$ can clearly be seen. . . . .	40
4.12	Nuclei along the isobaric chains $A = 66$ and $A = 70$ that could potentially contribute to the beam composition are marked with red squares. . . . .	41
4.13	The resulting $\beta$ -decay spectrum when bombarding the beam onto an aluminium stopper foil in logarithmic scale. $\gamma$ -ray transitions with energies up to 3.5 MeV are observed. . . . .	42
4.14	Number of nuclei as a function of time for $^{66}\text{Ge}$ ( $t_{1/2} = 2.26$ h) and $^{70}\text{Se}$ ( $t_{1/2} = 41$ min) for beam intensity $R = 1000$ and $N_{\text{Ge}}(t = 0) = N_{\text{Se}}(t = 0) = 0$ . The beam is on from $t = 0$ to 330 min. . . . .	44
4.15	The level scheme used in the GOSIA calculations for $^{66}\text{Ge}$ along with the known $\gamma$ -ray energies and matrix elements. . . . .	45

4.16	The level scheme used in the GOSIA calculations for $^{196}\text{Pt}$ along with the known $\gamma$ -ray energies and matrix elements. . . . .	46
4.17	Beam gated heavy-ion angular distributions showing experimental and calculated $\gamma$ ray yield integrated per 4 rings as a function of laboratory scattering angle, $\theta$ , for the de-excitation of the $2^+$ states in $^{66}\text{Ge}$ (left) and $^{196}\text{Pt}$ (right) . . . . .	47
4.18	Target gated heavy-ion angular distributions showing experimental and calculated $\gamma$ ray yield integrated per 3 rings as a function of laboratory scattering angle, $\theta$ , for the de-excitation of the $2^+$ states in $^{66}\text{Ge}$ (left) and $^{196}\text{Pt}$ (right) . . . . .	47
4.19	The coulomb cross section and excitation probability versus the labratory angles covered by the DSSSD. The cross section and excitation probability was calculated using GOSIA. . . . .	48
4.20	Beam gated non-Doppler spectra showing the number of counts for the 355 keV peak in $^{196}\text{Pt}$ . . . . .	49
4.21	Beam gated Doppler corrected spectra showing the counts for the 956 keV peak in $^{66}\text{Ge}$ . . . . .	49
4.22	kinematics plot of target recoil angles vs particle scattering angles for $^{66}\text{Ge}$ bombarding a $^{196}\text{Pt}$ target at 290.07 MeV. The kinematics was calculated using LISE++. . . . .	50
4.23	The coulomb cross section and excitation probability versus the recoil angles covered by the DSSSD. The cross section and excitation probability was calculated using GOSIA. . . . .	51
4.24	Variation of $\langle 2_1^+    E2    2_1^+ \rangle$ as a function of $\langle 2_1^+    E2    0_1^+ \rangle$ in $^{66}\text{Ge}$ . The solid black lines represent the loci from the upper and lower limits of the intensity ratio. The horizontal band represents the $1\sigma$ boundary for $\langle 2_1^+    E2    0_1^+ \rangle = 0.4827(15)$ eb. . . . .	52
5.1	Adopted $B(E2; 2_1^+ \rightarrow 0_1^+)$ values for even-even Ge isotopes. The $B(E2; 2_1^+ \rightarrow 0_1^+)$ value determined during this experiment is shown in comparison. . . . .	53
5.2	Adopted $B(E2; 2_1^+ \rightarrow 0_1^+)$ values for even-even Ge isotopes. The $B(E2; 2_1^+ \rightarrow 0_1^+)$ value determined during this experiment is shown in comparison. . . . .	54
5.3	Adopted $B(E2; 2_1^+ \rightarrow 0_1^+)$ values for even-even Ge isotopes. The $B(E2; 2_1^+ \rightarrow 0_1^+)$ value determined during this experiment is shown in comparison. . . . .	54
5.4	Adopted $B(E2; 2_1^+ \rightarrow 0_1^+)$ values for even-even Ge isotopes. The $B(E2; 2_1^+ \rightarrow 0_1^+)$ value determined during this experiment is shown in comparison. . . . .	55

# List of Tables

4.1	Position parameters used for the center of each MINIBALL triple cluster for the Doppler correction . . . . .	37
4.2	Observed $\gamma$ -ray transition energies following the corresponding $\beta$ -decay. . .	43

# Abbreviations

<b>CE</b>	Coulomb Excitation
<b>RE</b>	Reorientation Effect
<b>RDM</b>	Recoil Distance Method
National	Nuclear Data Center
<b>CM</b>	Center of Mass
<b>ISOL</b>	Isotope Separation On-Line
<b>PS</b>	Proton Synchrotron
<b>GPS</b>	General Purpose Separator
<b>HRS</b>	High Resolution Separator
<b>REX</b>	Radioactive beam EXperiment
<b>EBIS</b>	Electron Beam Ion Source
<b>RFQ</b>	Radio-Frequency Quadrupole accelerator
<b>IH</b>	Interdigital H structure
<b>MCP</b>	Multi-Channel Plate
<b>DSSSD</b>	Double Sided Silicone Strip Detector
<b>HPGe</b>	High-Purity Germanium
<b>DAQ</b>	Data Aquisition system
<b>DGF</b>	Digital Gamma Finder
<b>ADC</b>	Analog-to-Digital Converter
<b>MBS</b>	Multi Branch System

# Chapter 1

## Introduction

Until this day, the nuclear force and nuclear interactions are not completely understood. The study of nuclei and their properties based on their proton-neutron configuration is known as nuclear structure. Coulomb excitation (CE) experiments have played an important role in our understanding of fundamental properties of nuclei such as nuclear shape and nuclear collectivity. Coulomb excitation is the study of nuclei interacting solely through the electromagnetic interaction. Experimental precautions need to be taken with CE measurements to ensure that contributions from the nuclear interaction is negligible. The electric quadrupole moment of the ground state to the first excited state in even-even nuclei is the simplest nuclear shape studied in the laboratory frame. The electric quadrupole moment is a measurement of how much the nuclear charge acquires an ellipsoidal shape [17]. The electric quadrupole moment  $\hat{Q}$  is classically defined as:

$$\hat{Q} = \frac{1}{e} \sqrt{\frac{16\pi}{5}} \int r^2 Y_{20}(\theta, \phi) \rho(r) dV, \quad (1.1)$$

where  $e$  denotes the elementary charge,  $(r, \theta, \phi)$  is the nuclear spherical coordinates,  $\rho(r)$  is the nuclear charge density and  $Y_{20}$  is a spherical harmonic. The intrinsic quadrupole moment  $Q_0$  of a nuclear state is given by the expectation value of  $\hat{Q}$  with respect to the centre of mass frame. Whereas the spectroscopic quadrupole moment  $Q_s$ , is the expectation value of  $\hat{Q}$  with respect to the laboratory frame. In the centre of mass frame, the intrinsic quadrupole moment is defined as:

$$Q_0 = \int \rho(r) (3z^2 - r^2) dV, \quad (1.2)$$

where  $\rho(r)$  is the charge density of the infinitesimal volume  $dV$ ,  $r^2 = x^2 + y^2 + z^2$  is the distance to the volume  $dV$ , and  $z$  is the projection of  $r$  onto the symmetry axis

of the particle. If the charge density is concentrated along the  $z$ -direction, the term proportional to  $3z^2$  dominates,  $Q_0$  is positive and the particle is prolate. If the charge density is concentrated in the equatorial plane perpendicular to  $z$ , the term proportional to  $r^2$  dominates,  $Q_0$  is negative, and the particle is oblate. The intrinsic quadrupole moment  $Q_0$  must be distinguished from spectroscopic quadrupole moment  $Q_s$  in the laboratory frame. Due to angular momentum selection rules, a spin  $J = 1/2$  nucleus such as a nucleon, does not have a spectroscopic quadrupole moment; however, it may have a intrinsic quadrupole moment as was realized more than 50 years ago [6]. The reorientation effect (RE) provides a model independant way to determine  $Q_s$  of excited states with  $J \neq 0$  or  $J > 1/2$ . The RE generates a hyperfine splitting of the nuclear levels, which depends on the shape of the nuclear state and allows  $Q_s$  of a nucleus to be probed. To convert  $Q_s$  to  $Q_0$ , we need to make use of a nuclear model. One such model is the collective model, where the nucleus is assumed to be an axially symmetric rotor [6]. The relation between the intrinsic and spectroscopic quadrupole moments within the rotor model is given by:

$$Q_s(2_1^+) = \frac{3K^2 - J(J+1)}{(2J+3)(J+1)} Q_0(2_1^+), \quad (1.3)$$

where  $K$  is the projection of the total angular momentum onto the axis of symmetry and reduces to:

$$Q_s(2_1^+) = -\frac{2}{7} Q_0(2_1^+) \quad (1.4)$$

for  $K = 0$  and  $J = 2$ . The rotor model also relates the spectroscopic quadrupole moment to the reduce transition probability,  $B(E2; 0_1^+ \rightarrow 2_1^+)$ , for an electric excitation of multipole order 2 as follows []:

$$B(E2; 0_1^+ \rightarrow 2_1^+) = \frac{5}{16\pi} Q_0^2 |\langle I_1 K | 20 | I_2 K \rangle|^2, \quad (1.5)$$

which for  $K = 0$ ,  $I_1 = 0$  and  $I_2 = 2$ , the Clebsh-Gordan coefficient becomes 1 and Equation 1.5 reduces to:

$$B(E2; 0_1^+ \rightarrow 2_1^+) = \frac{5}{16\pi} Q_0^2. \quad (1.6)$$

## 1.1 Scientific motivation

The macroscopic properties of the atomic nucleus can drastically change when adding or removing a few nucleons. One such feature is the rapid evolution of nuclear evolution. Competing oblate and prolate shapes close to the ground state have been predicted and reported in a few regions on the nuclear chart [10, 24]. The region of light Kr and Se isotopes with  $N \sim Z$  is a region that displays rapid evolution of nuclear shapes. Along the Kr isotopic chain between  $N = 34 - 36$  and  $N = 32$  the shape changes from prolate to oblate [8, 13]. The same trend is observed along the Se isotopic chain between  $N = 34 - 36$  and  $N = 38$  [25, 31]. Shape coexistence is associated with the shape transition for the Kr isotopes [13, 20, 41]. There are indications of collective and noncollective modes in the low-energy spectra of the Ge isotopes. A systematic study of CE measurements for even-even Ge isotopes suggests that both a spherical and deformed shape coexist in one nucleus and reaches maximum mixing at  $^{72}\text{Ge}$  [27, 42]. The isotope  $^{66}\text{Ge}$  exhibits a very low  $B(E2; 2_1^+ \rightarrow 0_1^+)$  transitional strength when compared to its neighbouring nuclei. The systematics of the  $B(E2; 2_1^+ \rightarrow 0_1^+)$  values in  $^{66}\text{Ge}$  is given in Figure 1.1.

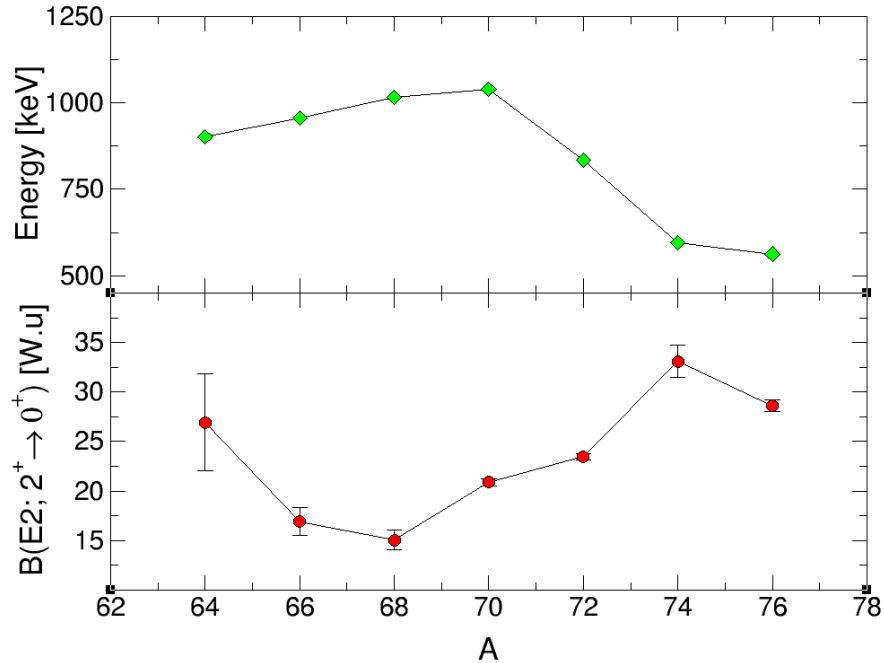


FIGURE 1.1: The  $2_1^+$  energy levels in keV for even-even Germanium isotopes from  $^{64}\text{Ge}$  to  $^{76}\text{Ge}$  (Top).  $B(E2; 2_1^+ \rightarrow 0_1^+)$  values for the same range of even-even Germanium nuclei.

The adjacent even-even nuclei,  $^{64}\text{Ge}$  and  $^{68}\text{Ge}$ , have been reported to be quite collective with transition strengths of  $B(E2; 2_1^+ \rightarrow 0_1^+) \sim 20$  W.u.. This decrease in collectivity

for  $^{66}\text{Ge}$  is also not reflected in the first  $2^+$  energy,  $E(2_1^+)$  as can be seen from Figure 1.1. Another curiosity is that fact that  $^{66}\text{Ge}$  exhibits an anomalously high  $2^+$  rotational parameter similar to the Se and Kr. The anomalous rise at  $J = 2$  in  $^{74-78}\text{Kr}$  has been attributed to the mixing of coexisting shapes. Low-lying excited  $0^+$  states have been observed in Se [19, 34, 43] and Kr [4, 8, 13] isotopes, which is a signature of shape coexistence in the nucleus [18, 24]. A tentative  $0_2^+$  state has been predicted for  $^{66}\text{Ge}$  but never observed before. Figure 1.2 shows the rotational parameter of  $^{66}\text{Ge}$  compared to Sr, Se and Kr isotopes.

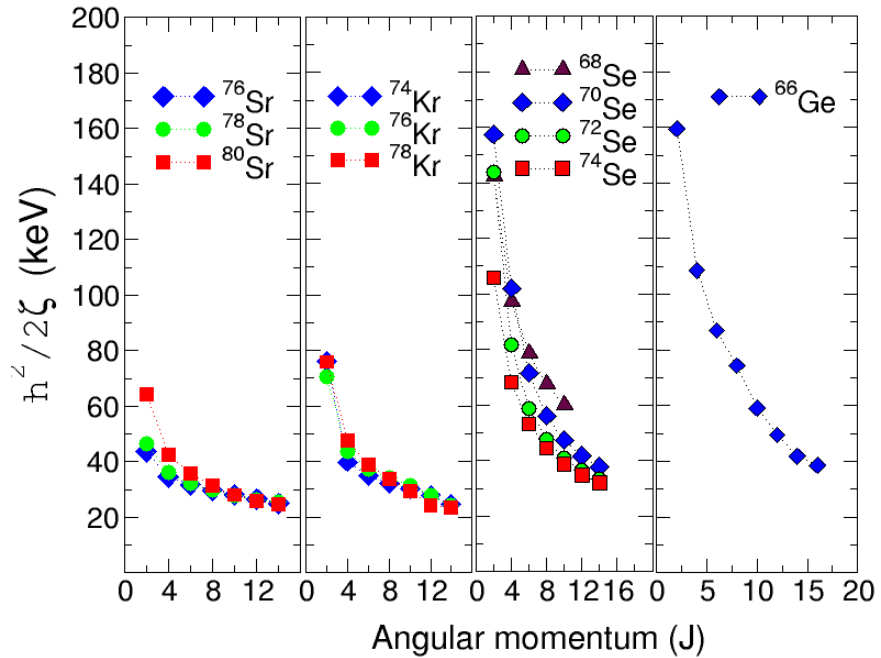


FIGURE 1.2: Comparison of rotational parameter for Sr, Kr, Se isotopes and  $^{66}\text{Ge}$  showing a similar trend.

To date, three measurements to determine the  $B(E2; 2_1^+ \rightarrow 0_1^+)$  for  $^{66}\text{Ge}$  has been carried out. The first was done by Wadsworth *et al* in 1979 using the Recoil Distance Method (RDM) [45]. For this experiment, the levels of  $^{66}\text{Ge}$  were populated via the  $^{58}\text{Ni}(^{10}\text{B}, p2\gamma)^{66}\text{Ge}$  reaction at a beam energy of 29 MeV. A mean lifetime of  $\tau = 5.3(10)$  ps was determined for the first  $2^+$  state at 956 keV resulting in a  $B(E2; 2_1^+ \rightarrow 0_1^+) = 12.0(23)$  W.u.. The second measurement was performed by Luttko *et al*, in 2012 which also used the RDM [33]. Excited states in  $^{66}\text{Ge}$  were populated by using the  $^{58}\text{Ni}(^{10}\text{B}, p2n)^{66}\text{Ge}$  reaction at a beam energy of 28 MeV. The lifetime of the first  $2^+$  state in  $^{66}\text{Ge}$  was determined through a direct gate on the  $4_1^+ \rightarrow 2_1^+$  transition at 1217 keV. A mean lifetime of  $\tau = 3.8(5)$  ps was determined for the first  $2^+$  state and a  $B(E2; 2_1^+ \rightarrow 0_1^+) = 16.9(22)$  W.u. was calculated from this lifetime. The final measurement was performed by Corsi *et al* using intermediate CE in 2013 [16]. A cocktail beam consisting of  $^{68}\text{Se}$  (12%),  $^{67}\text{As}$  (41%) and  $^{66}\text{Ge}$  (30%) was produced by fragmentation of

a  $^{78}\text{Kr}$  primary beam at 150 Mev/u onto a 329 mg/cm<sup>2</sup> thick  $^9\text{B}$  production target. The secondary beam was bombarded onto a 257 mg/cm<sup>2</sup> thick  $^{197}\text{Au}$  target with a beam energy of 79 MeV for CE. A value of  $B(E2; 2_1^+ \rightarrow 0_1^+) = 17.68(0.8)$  W.u. was determined by this experiment.

In 2016, Pritychenko *et al* compiled experimental  $B(E2; 2_1^+ \rightarrow 0_1^+)$  values for 447 even-even nuclei [39]. The previously mentioned  $B(E2; 2_1^+ \rightarrow 0_1^+)$  values were used to perform a weighted average resulting in a value of  $B(E2; 0_1^+ \rightarrow 2_1^+) = 16.9(14)$  W.u.. This new weighted average is currently the accepted value for  $^{66}\text{Ge}$  in the National Nuclear Data Center (NNDC) [11]. These  $B(E2)$  values can be used to calculate the magnitude of  $Q_s$  using the rotor model, but in order to determine the sign of the quadrupole moment, RE technique needs to be used.

## Chapter 2

# Coulomb Excitation Theory

Since CE theory was introduced in the late 1950s [2], it has allowed collective quadrupole properties of many stable nuclei to be measured. Coulomb excitation has also allowed the majority of the known transition probabilities and deformation properties of atomic nuclei to be determined. This technique is especially favoured for exotic radioactive isotopes because it provides a tool to probe the  $B(\sigma\lambda)$  value and potentially quadrupole moments. Coulomb excitation is the excitation of a nucleus via the time-dependent electromagnetic field induced by a collision with another nucleus. If this interaction takes place well below the Coulomb barrier, the distance between the interacting nuclei are larger than the range of the nuclear force. This safety condition ensures that effects from the nuclear force are negligible and the interaction takes place only via the well understood electromagnetic force [1]. If this condition is met multipole matrix elements which characterises the electromagnetic decay of the states of the states involved can also be used to express the CE reaction cross section. A determination of the CE reaction cross section allows for the study of electromagnetic properties of low-lying states as well as extracting fundamental nuclear structure information including the spectroscopic quadrupole moment  $Q_s(J^\pi)$  of an excited state. The spectroscopic quadrupole moment provides a way to measure the nuclear charge distribution of a nucleus in the laboratory frame. One of the important aspects of this technique is the population of magnetic substates depending on the quadrupole shape of the state. This is known as the “Reorientation effect”. The angular distribution of the de-excited  $\gamma$  rays as a function of scattering angle may be enhanced ( $Q_s(2_1^+) > 0$ ) or inhibited ( $Q_s(2_1^+) < 0$ ), hence providing a probe of the spectroscopic quadrupole moment  $Q_s$ . The difference in the magnetic substate population depends on whether the shape is prolate, oblate or spherical. An illustration of these shapes are depicted in Figure 2.1.

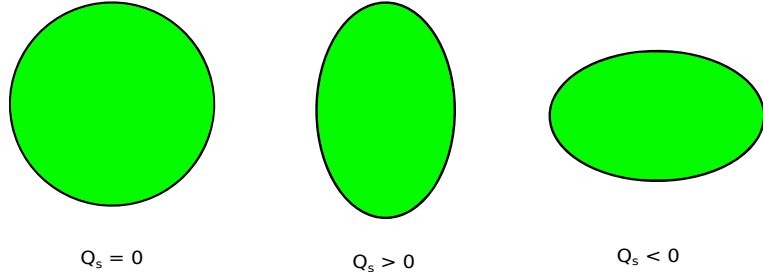


FIGURE 2.1: Nuclear shapes based on the value of the spectroscopic quadrupole moment  $Q_s$ .

This dependence on the shape of the nucleus provides a means to determine  $Q_s$  by measuring the CE reaction cross section or integrated  $\gamma$  rays as a function of scattering angle [1]. The theory of CE is discussed extensively in [1, 2, 5]. This Chapter provides a brief description of the relevant theory to determine the spectroscopic quadrupole moment in Section 2.1 and is followed by a description of the CE analysis code Gosia in Section 2.2.

## 2.1 Theory Description

A projectile nucleus with atomic mass  $Z_p$  is guided onto a target nucleus with atomic mass  $Z_t$ . If the energy of the projectile nucleus  $E_p$  is well below the Coulomb barrier, the distance of closest approach  $b(\theta)$  will be large enough to ensure no nuclear contributions are present in the interaction. This is illustrated using a picture of a classical Rutherford scattering experiment shown in Figure 2.2.

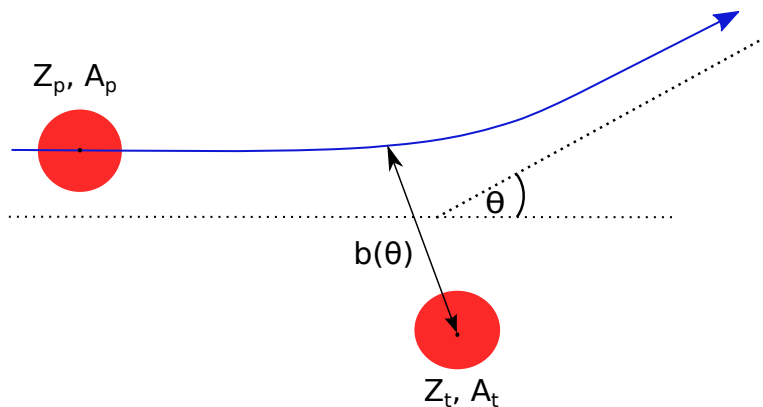


FIGURE 2.2: A CE scattering event in the LAB frame. At the point of closest approach  $b$ , the interaction potential is the strongest. The hypobolic path which the projectile follows is illustrated by the blue arrow.

The strongest point of interaction is reached at the distance of closest approach  $b(\theta)$ , where the excitation probability is the highest. To obtain the total excitation probability, the complete particle trajectory has to be included in the calculation as the Coulomb force is a long-range force. This boundary condition and the fact that the theory of electromagnetic is well understood allow for an accurate calculation of both single- as well as multiple-step excitations. In order for the interaction between the projectile and target to take place solely via the well-known electromagnetic force, the maximum bombarding energy should be below the height of the Coulomb Barrier [5]. Studies on the effects of coulomb and nuclear interference have been carried out to estimate the maximum "safe" bombarding energy,  $E_{max}$ , using the masses and charges of the interacting nuclei [2]. The safe bombarding energy for any projectile and target combination can be determined using the classical expression of the minimum distances separating the nuclear surfaces  $S(\vartheta)_{min}$  given by

$$S(\vartheta)_{min} = \frac{0.72Z_pZ_t}{E_{max}}(1 + \frac{A_p}{A_t})[1 + \csc(\frac{\vartheta}{2})] - R_0(A_p^{1/3} + A_t^{1/3})fm \quad (2.1)$$

where  $R_0 = 1.25fm$  is the average nucleon radius,  $A_{p/t}$  and  $Z_{p/t}$  is the mass and charge respectively of the projectile nucleus ( $p$ ) and the target ( $t$ ) and  $E_{max}$  is the maximum bombarding energy of the projectile. This minimum distance has been shown to be 5 fm to ensure that only 0.1% of the total interactions are due to the nuclear force [14]. This gives rise to an expression for the distance of closest approach,

$$R_0(A_p^{\frac{1}{3}} + A_t^{\frac{1}{3}}) + 5 > b = \frac{Z_pZ_te^2}{E_p} \quad (2.2)$$

where  $E_p$  is the kinetic energy of the projectile. The theory relies upon first and second order perturbation theory to describe a one or two step process making it relatively easy to study properties in light-ion beams. Study of heavier beams with many states presents a complexity problem that needs to be solved using a numerical method. This complexity gave rise to GOSIA, the CE code which will be discussed in Section 2.2.

### 2.1.1 Semiclassical approximation

Coulomb excitation theory can be treated in two ways. The first is a fully quantum mechanical approach as is discussed in [1]. It can also be treated using a semiclassical approximation in which the whole scattering and excitation process follows the classical Rutherford trajectories. The electromagnetic excitation has a negligible effect on the trajectories and is treated fully quantum mechanically. The semiclassical picture is

justified if two conditions are met. Firstly, the particle needs to be described by a wave packet whose dimensions are small compared with the distance of closest approach. This condition is satisfied when the Sommerfeld parameter,  $\eta$ , is much greater than unity:

$$\eta = \frac{2\pi a}{\lambda} = \frac{Z_p Z_t e^2}{\hbar v_p}, \quad (2.3)$$

where  $a = b/2$ , half the distance of closest approach,  $\lambda$  is the de Broglie wavelength of the projectile with a velocity of  $v_p$ ,  $Z_p e$  and  $Z_t e$  are the respective charges of the projectile and target nucleus. The strong repulsive Coulomb interaction between the projectile and target nucleus implied by  $\lambda \gg 1$  then also guarantees that the projectile will not penetrate into the target nucleus. Secondly, the energy loss of the impinging particle needs to be small when compared to the bombarding energy. The hyperbolic trajectory that the projectile follows in the semiclassical approximation can only be true if the incoming energy and outgoing energy is similar. This implies that the inelastic scattering can be used to approximate elastic scattering with the energy loss being negligible. Since the energy transfer between the projectile and target can occur at any point along the path of the trajectory, the energy loss of the impinging particle need to be small relative to the center-of-mass (CM) energy. This condition can be expressed as [2]

$$\frac{\Delta E}{E} \ll 1 \quad (2.4)$$

where CM energy is given by  $E = \frac{1}{2}m_0v_b^2$  and  $m_0$  is the reduced mass. It is also useful to define the adiabaticity parameter  $\xi$  as the difference between the incoming  $\eta_i$ , and outgoing  $\eta_f$ ,

$$\xi = \eta_i - \eta_f = \frac{Z_p Z_t A_p^{1/2} \Delta E}{12.65 E^{3/2}} = \frac{\eta \Delta E}{2E_p}. \quad (2.5)$$

For  $\xi \leq 1$  and small value of  $\Delta E$ , a large excitation probability is expected, whereas for  $\xi \gg 1$  a vanishing excitation cross section will be the case, because high  $\Delta E$  hampers CE [9]. Furthermore,  $\xi$  can also be interpreted as the ratio of the collision time relative to the lifetime of the nuclear state being excited:

$$\xi = \frac{t_{\text{collision}}}{\tau_{\text{nuclear}}} = \frac{a \Delta E}{\hbar v}, \quad (2.6)$$

where the lifetime of the nuclear state,  $\tau$  can be calculated using the uncertainty principle,

$$\tau = \frac{h}{\Delta E}. \quad (2.7)$$

With both the conditions justifying the semiclassical approximation satisfied, it is valid for the analysis of heavy ion CE. In this approach, the Rutherford cross section  $\sigma_R$ , associated with the projectiles motion is described by

$$d\sigma_R = \frac{1}{4} a^2 \sin\left(\frac{\vartheta}{2}\right)^{-4} d\Omega, \quad (2.8)$$

where  $\vartheta$  is the CM scattering angle and  $a$  is half the distance of closest approach. If during the collision the nucleus undergoes a transition from an initial state  $|i\rangle$  to a final state  $|f\rangle$ , the CE cross section may be related to the Rutherford cross section by

$$d\sigma_f = P_{if} d\sigma_R, \quad (2.9)$$

where  $P_{if}$  is the probability the nucleus is excited in the collision and scatters into the solid angle  $d\Omega$ . The probability  $P_{if}$  is expressed as

$$P_{if} = \frac{1}{2I_i + 1} \sum_{M_i M_f} |a_{if}|^2, \quad (2.10)$$

where  $a_{if}$  are the transition probabilities for exciting a nucleus from the ground state with spin  $I_i$  to a final state with spin  $I_f$ ,  $M_i$  and  $M_f$  are the magnetic substates quantum numbers of the initial and final states respectively. Perturbation treatment of the semiclassical approximation provides a way to understand the excitation process. For CE involving light-ions,  $P_{if}$  is less than unity and first-order perturbation treatment for the excitation process may be adequate. Heavier targets in scattering experiments enhance second and higher-order terms in the perturbation expansion of the CE cross section and, hence, higher order perturbation theory is necessary. Magnetic transitions are hindered by a factor of  $v/c$  when compared to electric transitions of the same multipole order and can therefore be disregarded in the perturbation treatment.

### 2.1.2 First-order Perturbation Theory

First-order perturbation may be used to evaluate the excitation amplitudes of the Coulomb excited states given that higher-order contributions or couplings are negligible. The first-order perturbation treatment of the cross-sections describes the interaction

taking place between the electromagnetic field and the system of nuclear charges of the collision partners involved. This approach yields reasonable estimates for the excitation amplitude and cross sections of nuclei with final state  $|f\rangle$  which are strongly coupled to the initial state  $|i\rangle$  through a large matrix element, with  $|f\rangle$  is not strongly coupled to any other high-lying states. This is illustrated in Figure 2.3.

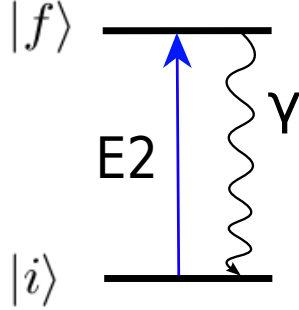


FIGURE 2.3: A one-step excitation from an intial state  $|i\rangle$  to a final state  $|f\rangle$ , with the excitation and deexcitation clearly shown. In this case, a E2 transition in a even-even nuclei is observed.

A simple way to express the excitation process for CE is to treat it as a first order perturbation [1] of the time-dependant Schrödinger equation of the form:

$$i\hbar \frac{\partial}{\partial t} |\psi(t)\rangle = H(t) |\psi(t)\rangle, \quad (2.11)$$

where the Hamiltonian  $H(t)$ , can be seperated into three parts of the electromagnetic interaction. The first is the monopole-monopole term  $H_0(t)$ , which treats the Rutherford scattering and the classical trajectories. The second term is the monopole-multipole term  $V(r(t, \theta, \phi))$ , which is responsible for the excitation of either collision partner. The third term is the multipole-multipole term which is responsible for the excitation of both the target and projectile nuclei simultaneously. The probability of exciting both the projectile and target is negligible compared to the excitation of a single collision partner and can therefore be excluded from the Hamiltonian. The Hamiltonian can then be expressed as

$$H(r(t)) = H_0(r(t)) + V(r(t)). \quad (2.12)$$

The time-dependant interaction potential  $V(r(t))$  originating from one collision partner influencing the second is used to calculate the excitation probabilities along the whole trajectory [35]. From first-order time-dependant perturbation theory the excitation amplitudes may be expressed as

$$a_{if} = \frac{1}{\hbar} \int_{-\infty}^{\infty} \langle f | V(r(t)) | i \rangle e^{i\omega_{if} t} dt, \quad (2.13)$$

where  $\omega = \Delta E / \hbar$  and  $\Delta E = E_f - E_i$  is the excitation energy for a transition from an initial state with energy  $E_i$  to a final state with an energy  $E_f$ . Performing a multipole expansion on the monopole-multipole term allows the excitation amplitudes  $a_{if}$  to be evaluated. The interaction responsible for electric multipole transitions is defined in [1] as

$$V(r(t)) = 4\pi Z' e \sum_{\lambda=1}^{\infty} \sum_{\mu=-\lambda}^{\lambda} \frac{(-1)^{\mu}}{2\lambda+1} M(E\lambda, \mu) Y_{\lambda\mu}(\theta, \phi) r^{-\lambda-1} \quad (2.14)$$

where  $\lambda$  and  $\mu$  are the multipole order of the excitation,  $Z'$  is the atomic number of the other collision partner,  $Y_{\lambda\mu}(\theta, \phi)$  are the spherical harmonics with angles  $\theta$  and  $\phi$  given in the center of mass frame, and  $M(E\lambda, \mu)$  is the electric multipole operator which is defined as

$$M(E\lambda, \mu) = \int r^{\lambda} Y_{\lambda\mu}(\theta, \phi) \rho(r) d\tau, \quad (2.15)$$

where  $\rho(r)$  is the nuclear charge density. At this point, we can neglect the magnetic multipoles since magnetic excitation scales with a factor of  $(v/c)^2$  and are much smaller than their electric counterparts in the non-relativistic case. The transition amplitudes can be evaluated by substituting Equation 2.14 into Equation 2.13, yielding

$$a_{if} = \frac{4\pi Z' e}{i\hbar} (-1)^{\mu} S_{\mu\lambda} \langle I_i M_i | M(E\lambda, \mu) | I_f M_f \rangle, \quad (2.16)$$

where  $S_{\mu\lambda}$  denotes the orbital integral along the classical trajectory  $r$  give by:

$$S_{\mu\lambda} = \int_{-\infty}^{\infty} e^{i\omega t} Y_{\lambda\mu}(\theta(t), \phi(t)) [r(t)]^{-\lambda-1} dt. \quad (2.17)$$

### Coulomb Excitation

The reduced matrix elements of the electric nuclear moments can be given by the Wigner-Eckart theorem,

$$\langle I_i M_i | M(E\lambda, \mu) | I_f M_f \rangle = (-1)^{I_i - M_i} \frac{1}{2} \langle I_f || M(E\lambda) || I_i \rangle. \quad (2.18)$$

These reduced transition elements are related to the transition strengths  $B(E\lambda)$  and such that the reduced transition probability may be written as

$$B(E\lambda; I_i \rightarrow I_f) = (2I_i + 1)^{-1} |\langle I_i || M(E\lambda) || I_f \rangle|^2. \quad (2.19)$$

The CE cross section for electric excitations may then be expressed as

$$\sigma_{E\lambda} = \frac{Z'e^2}{\hbar v} a^{-2\lambda+2} B(E\lambda) f_{E\lambda}(\xi), \quad (2.20)$$

where  $f_{E\lambda}(\xi)$  is the dimensionless CE function containing all the information about the classical trajectory of the scattered particles. The values for  $f_{E\lambda}(\xi)$  are tabulated in [1]. The total CE cross section expressed in Equation 2.20 is directly proportional to the reduced transition probabilities expressed in Equation 2.19.

### 2.1.3 Second-order Perturbation Theory

In the framework of first-order perturbation theory, excitation amplitudes are typically quite small:  $a_{if} \ll 1$ . For heavy-ion collisions, the transition probability increases with ion energy and, thus, the condition  $a_{if} \ll 1$  may no longer be satisfied and second-order effects have to be considered. Two consequences arise from this condition; first-order transition probabilities may be affected by second-order terms and states which were previously not accessible may be populated using multi-step excitations [1]. To account for second-order effects, the excitation needs to be treated using second-order perturbation theory while still maintaining the classical trajectories. A second excited state  $|f\rangle$  may be reached through the excitation of an intermediate state  $|m\rangle$ , from an initial state  $|i\rangle$  given by

$$a_{if}^{(2)} = a_{if}^{(1)} + a_{imf}^{(1,2)}, \quad (2.21)$$

where  $a_{if}^{(1)}$  is defined in Equation 2.13 and  $a_{imf}^{(1,2)}$  is the amplitude of the transition from the intermediate state to the final state given by

$$a_{imf}^{(1,2)} = \frac{1}{i\hbar} \int_{-\infty}^{\infty} \langle f | V(r(t)) | m \rangle e^{i\omega_{mf} t} \times \langle m | V(r(t)) | i \rangle e^{i\omega_{im} t} dt. \quad (2.22)$$

These first-order and second-order processes interfere with each other and therefore have to be included into the calculation regardless of how small the probability of the multi-step excitation may be. This interference leads to a phenomenon known as the RE. This

effect, which is typically observed in E2 transitions of even-even nuclei occurs when the intermediate state  $|m\rangle$  and the final state  $|f\rangle$  in a multi-step excitation are magnetic substates of the same excited state. The RE is illustrated in Figure 2.4.

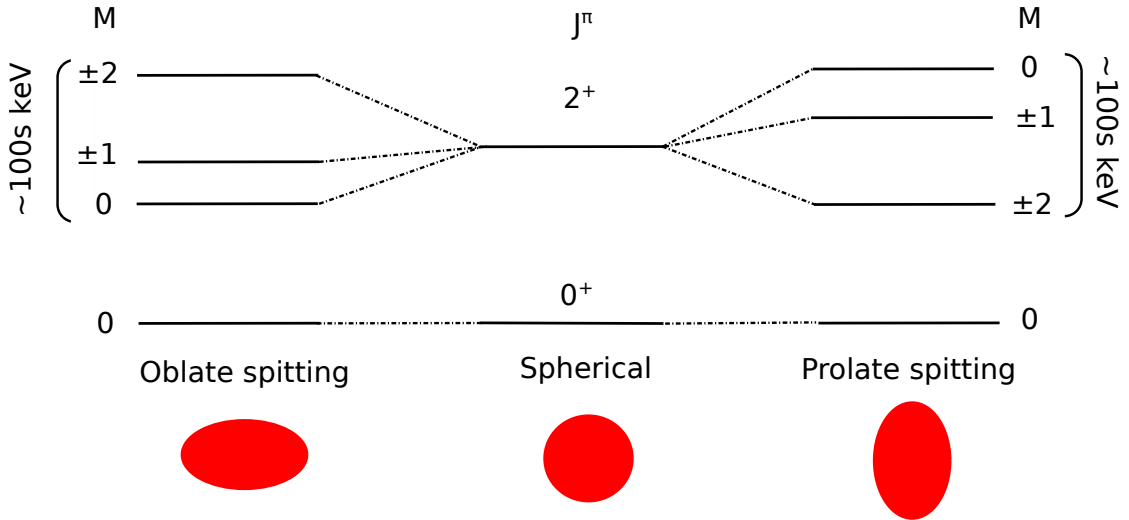


FIGURE 2.4: Schematic representation of the reorientation effect. The final state  $|f\rangle$  can be reached via an intermediate state  $|m\rangle$ . The final state can be one of the magnetic substates of the excited state. The splitting of the energy levels that the magnetic substates can take on is dependant on the static quadrupole moment by the relation  $E(t) \sim eQ_s Z/r^3(t)$ .

From Equation 2.21, it can be seen that the excitation amplitude of a state  $k$  depends on the coupling of all  $n$  states. This, in turn, means the the reduced matrix elements defined in Equation 2.18 is coupled for all  $n$  states. A numerical approach is needed to solve this complex system of coupled differential equations.

## 2.2 Gosia

Advances in the semi-classical theory for multiple CE has led to the development of computer programs which could solve the vast amount of coupled differential equations numerically. The first of these numerical minimization programs is known as COULEX, developed by Winther and de Boer [48]. The input of this code is a set of initial matrix elements, level schemes of the nuclei involved in the collision and the experimental details such as beam energy. The program then computes the angular distribution of the  $\gamma$ -rays by integrating the many differential equations involved in the excitation. The calculations have to be corrected for the transfer of energy to excite the nucleus as well as for systematic errors. This correction is achieved by introducing symmetrized orbits in the semi-classical calculations. The calculated and measured yields can be made to agree with each other by manually varying the model-dependent parameters. This

model-dependency proved to be of concern for semi-classical multiple CE calculations where a large number of reduced matrix elements could contribute significantly to the excitation of a single state. The introduction of Gosia, in 1980, overcame this model-dependency as well as other issues such as treating higher multiple orders [15].

Gosia accepts a set of electric (E1-E6) and magnetic (M1 and M2) multipole matrix elements and calculates the excitation cross section for multiple excitations. It can be used for simulating an experiment by determining optimum angles and beam/target combinations to use in an experiment. Gosia can also be used to analyse real data by fitting matrix elements independently to a number of data. The  $\gamma$ -ray yield of a given transition, following the de-excitation of a state populated during the collision, is the most important observable. It allows the excitation and decay to be compared since the matrix elements that govern the decay of these populated states are the same matrix elements which determine the excitation. Gosia also allows for independent data, such as lifetimes of excited states, known matrix elements, branching ratios and E2/M1 mixing ratios, to be included in the fit. A numerical integration of the coupled-channel differential equations is performed to calculate the cross-section and consequently the  $\gamma$ -ray yields [15].

The calculation is done at a single value for energy and angle and is referred to as the "point yield", given by

$$Y_{point}(I \rightarrow I_f, \theta_p, E) = \sin(\theta_p) \int_{\phi_p} \frac{d^2\sigma(I \rightarrow I_f)}{d\Omega_\gamma d\Omega_p} d\phi_p. \quad (2.23)$$

The integrated yields are calculated by integrating over the entire solid angle and the range of bombarding energies resulting from the energy loss in the target, given by

$$Y_{int}(I \rightarrow I_f) = \int_{E_{min}}^{E_{max}} dE \frac{1}{(\frac{dE}{dx})} \int_{\theta_{p,min}}^{\theta_{p,max}} Y_{point}(I \rightarrow I_f) d\theta_p, \quad (2.24)$$

where  $\frac{dE}{dx}$  is the stopping power of the target material obtained using SRIM [49]. Equation 2.24 includes the Rutherford cross-section and the solid angle factor  $\sin(\theta_p)$ .

Computing Equations 2.23 and 2.24 for many angles and energies can be time consuming. To speed up this process, Gosia makes use of yields calculated over an average bombarding energy and an average scattering angle. These average point yields are corrected by a constant factor calculated along with the integration. The integration along with the recalculation of the correction factor only needs to take place again if the matrix elements diverge significantly. The correction constant is given by

$$Y_{exp}^c(I \rightarrow I_f) = Y_{exp}(I \rightarrow I_f) \frac{Y_{point}(I \rightarrow I_f)}{Y_{int}(I \rightarrow I_f)}, \quad (2.25)$$

where  $Y_{exp}(I \rightarrow I_f)$  is the experimental yields. The fitting of the matrix elements is performed by locating a  $\chi^2$  minimum in Equation 2.24 given by

$$\chi^2 = \frac{1}{N} \sum_i \left( \frac{Y_{exp}(i) - Y_{exp}^c(i)}{\Delta Y_{exp}(i)} \right)^2, \quad (2.26)$$

where  $Y_{exp}(i)$  are the experimental yields,  $\Delta Y_{exp}(i)$  are the errors in the experimental yields and N is the number of data points used in the integration.

# Chapter 3

## Experimental Methodology

The CE of the unstable nucleus  $^{66}\text{Ge}$  was performed in 2017 at the ISOLDE facility at CERN in Switzerland. This chapter details the experimental methodology used to obtain the necessary beam parameters as well as the equipment used to successfully perform the CE experiment. Section 3.1 discusses the beam production process at the HIE-ISOLDE facility and Section 3.2 discusses MINIBALL, the array of High Purity Germanium (HPGe) detectors used to perform the measurement.

### 3.1 ISOLDE facility

The ISOLDE facility, based at CERN in Geneva, Switzerland, is a rare isotope production facility. The ISOLDE facility utilizes the “Isotope Separation On-Line” (ISOL) technique, one of the commonly used methods applied to study low-energy properties of exotic nuclei. This method allows for the production of both neutron-rich as well as proton-rich nuclei with very low recoil velocity. To produce the necessary beam, the following steps associated with the ISOL method must be taken; (*i*) a thick heavy target is bombarded with protons, (*ii*) the diffusion of nuclei out of the primary target into an ion source, (*iii*) ionization, extraction and mass separation of the desired beam. The following sections discuss the beam production and post-acceleration process in detail. Figure 3.1 shows an illustration of the layout of the ISOLDE facility as it stands to date.

#### 3.1.1 Isotope Production

The beam production at ISOLDE starts with a beam of high energy protons received from Proton Synchrotron (PS) Booster with an energy of 1.4 GeV. The protons are guided from the PS Booster to ISOLDE in pulses with a minimum spacing of 1.2 s

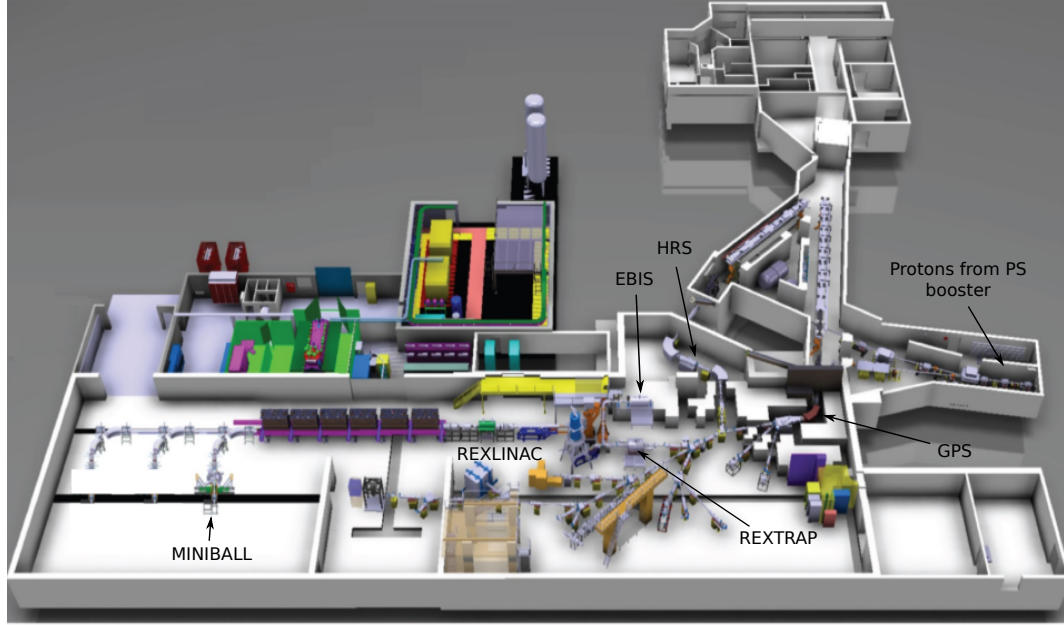


FIGURE 3.1: Schematic overview of the ISOLDE facility after the HIE-ISOLDE upgrades. There are many experimental setups in the ISOLDE hall, only those used during this experiment have been labelled.

between pulses. Each pulse is able to reach a maximum intensity of  $3.2 \times 10^{13}$  ions/s, which would result in a maximum intergrated intensity of  $4 \mu\text{A}$ . However, due to safety regulations, the spacing between pulses are increased to 2.4 s such that the average intergrated intensity amounts to  $2 \mu\text{A}$  [28]. These proton beams are then guided to one of two primary targets, each coupled to a different mass separator. The target can be stored inside the target chamber, usually consisting of graphite or tantalum, in one of the following forms; powder, metal, molten metal or pills of carbon fibers. Many parameters have to be considered when choosing the target material to ensure that the maximum beam intensity of the requested isotope may be delivered. These properties are the production cross section, release characteristics, density, mechanical and thermal resistance, melting point, target structure and electrical conductance to name a few.

The impingement of the high energy proton beam onto the thick primary target produces a variety of radioactive isotopes via fission, fragmentation and spallation processes. In approximately 70% of the cases,  $^{238}\text{UC}_x$  is used as a primary target. The beam intensity may be increased by heating the target which enhances effusion and diffusion processes. Another consideration is that of extracting the required isotope as a molecular beam. The molecular beam approach allows for purer beams of the required isotope to be extracted. Knowledge of the chemical properties of the desired isotope are required, such that a molecule consisting predominately of the desired isotope may be created. This approach also reduces possible contaminants as the production of a chemical compound

with the remaining isotopes are suppressed. The primary target used in this experiment was  $\text{ZrO}_2$ , which was intended to produce  $^{70}\text{SeCO}$  molecules. However, the sulphur in the primary target allowed for the production of  $^{66}\text{GeS}$  molecules in excess to that of selenium. This ratio kept increasing in favour of  $^{66}\text{GeS}$  inevitably resulting in a beam of  $^{66}\text{Ge}$ . The ionization of the molecules was done using surface ionization, whereby the transfer line, usually made of tungsten or tantalum, was heated to strip electrons from the desired molecules. This is possible due to the fact that germanium has a lower thermionic work function to that of tungsten or tantalum. The ionized molecules ( $1^+$  charge state) are then extracted from the target-ion source by applying a 30 to 60 kV external electrostatic potential. After this extraction process, the desired molecules need to be selected and guided to the experimental setup. This selectivity is achieved using the mass-over-charge ratio ( $A/q$ ) with the use of two different mass separators; the General Purpose Separator (GPS) and the High Resolution Separator (HRS). Figure 3.2 depicts the beam line layout in the ISOLDE hall, showing the HRS and GPS mass separators.

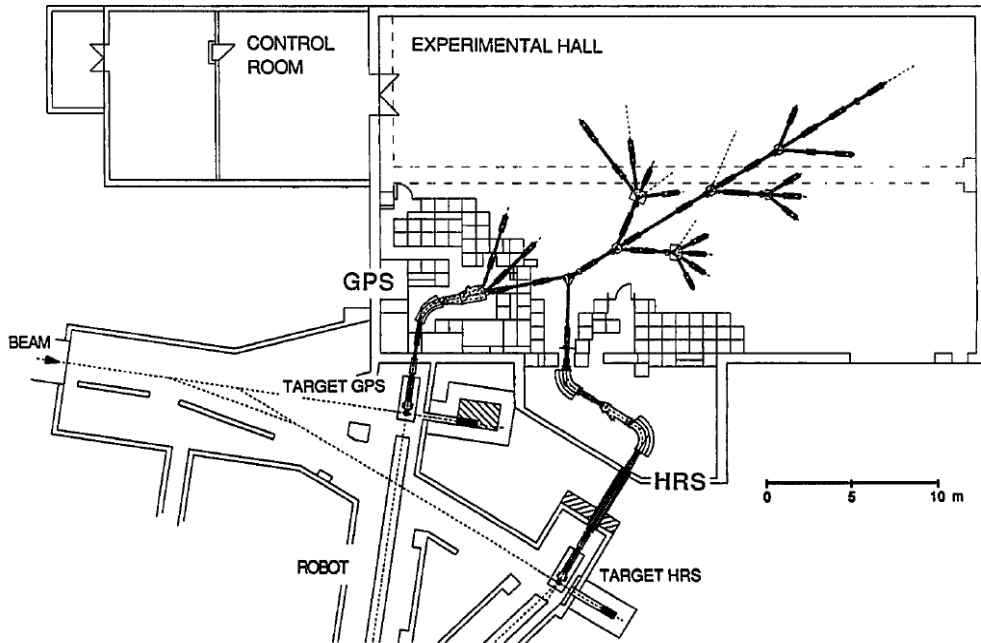


FIGURE 3.2: Schematic overview of the beam line layout in the ISOLDE hall. Both the HRS and GPS mass separators are illustrated [29].

Each mass separator is connected to its own target station, allowing for very flexible beam delivery. These mass separators feed one common beam line which delivers the beam to the majority of the available experimental setups in the ISOLDE facility. The following subsection gives more detail about GPS since it was the mass separator used for this experiment. Refer to [28] for a more detailed description of HRS.

### 3.1.1.1 GPS

The General Purpose Separator is the smaller of the two isotope separators available at the ISOLDE facility. It comprises of two electrostatic quadrupole lenses followed by a double focusing  $70^\circ$  magnetic with a mean bending radius of 1.5 m. The analyzing magnet is followed by the switchyard which is located in the focal plane and allows for the selection of three ion beams within a mass range of  $\pm 15\%$  from the central mass [28]. It also allows for these three beams to be delivered to any experiment in the experimental hall simultaneously. The switchyard is made of pairs of electrostatic cylinder-shaped deflector plates, one on either side of the central mass. The selection of the mass is achieved by moving the deflector plates parallel to the focal plane. Figure 3.3 shows a picture of the switchyard used in GPS.

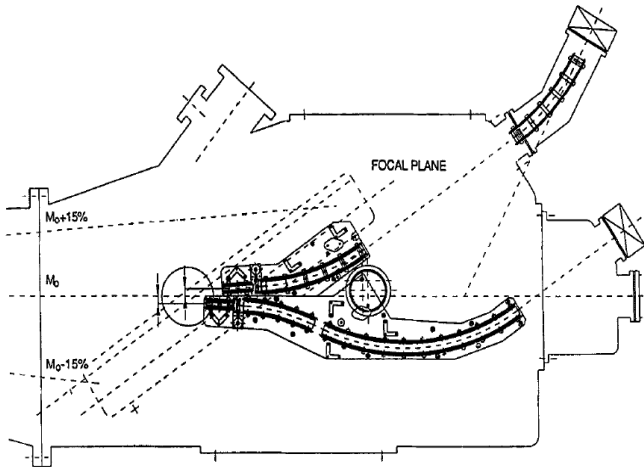


FIGURE 3.3: The GPS switchyard [29].

### 3.1.2 Post-acceleration

The radioactive ion beam is delivered with an initial beam energy of 30 – 60 keV to the various low energy experimental setups in ISOLDE’s experimental hall. The Radioactive beam EXperiment (REX) was designed to further accelerate beams from ISOLDE to beam energies of up to 3.0 MeV/u. The post-acceleration unit comprises of a penning trap for deacceleration and bunching of the beam, followed by a charge breeding system. This process allows for a compact accelerator to be used to accelerate beams to moderate energies without the need for a large-scale accelerator. Figure 3.4 shows a schematic overview of the REX-ISOLDE. The following sections will describe in more detail each of the components that makes up the post-acceleration process.

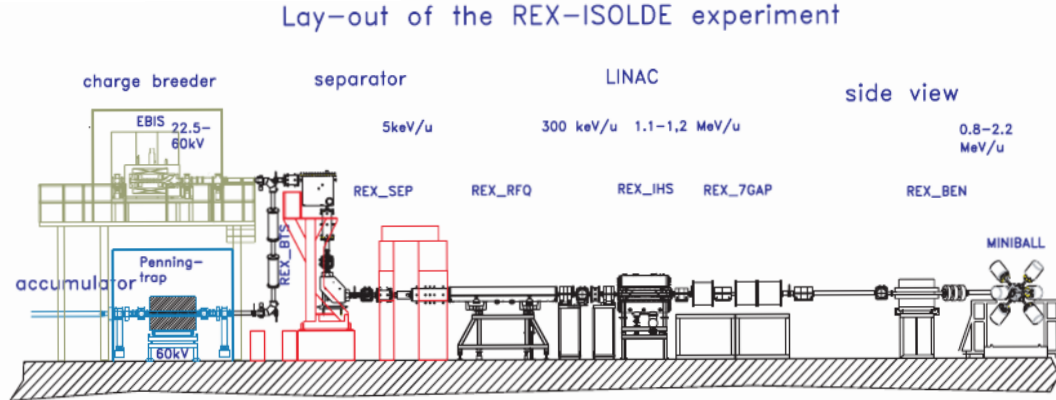


FIGURE 3.4: A detailed layout of REX-ISOLDE. [23].

### 3.1.2.1 REXTRAP

The singly-charge ion beam from GPS is injected into REXTRAP, a penning trap designed to cool and bunch the ions. REXTRAP is shown on the left in Figure 3.5. REXTRAP consists of two regions; one for stopping the ions and the other to trap them. Both these regions are typically filled with neon or argon as a buffer gas [22]. Incoming ions are cooled by collisions with the buffer gas and trapped by an applied High-Voltage (HV) field. To further increase the energy loss of the ions, the pressure in the trapping region is an order of magnitude lower than that of the stopping region. In addition, an applied 3 T magnetic field allows for the confinement of the ions in the center of the trap. Within the applied electric and magnetic fields, the ions are forced into a magnetron motion around the trap center, a reduced cyclotron motion and an axial motion (harmonic oscillation). The collisions with the buffer gas disrupt the magnetron motion of the ions and increase their orbit. Recentering of the ions of interest is achieved by applying a radio-frequency field with a cyclotron frequency that matches the desired ions mass.

### 3.1.2.2 REXEBIS

At this point of the post-acceleration, the beam has been deaccelerated and bunched. It then gets injected into the Electron Beam Ion Source (EBIS) for charge breeding [47]. REXEBIS is shown on the right in Figure 3.5. The charge breeding process is essential to achieve a beam energy of 5.5 MeV/u with the subsequent compact linear accelerator. The charge breeding in EBIS is achieved through electron impact. The incoming ions are confined within a trapping region and bombarded with an electron beam. The electron beam, typically 3-6 keV with a current of 200 mA, is provided by

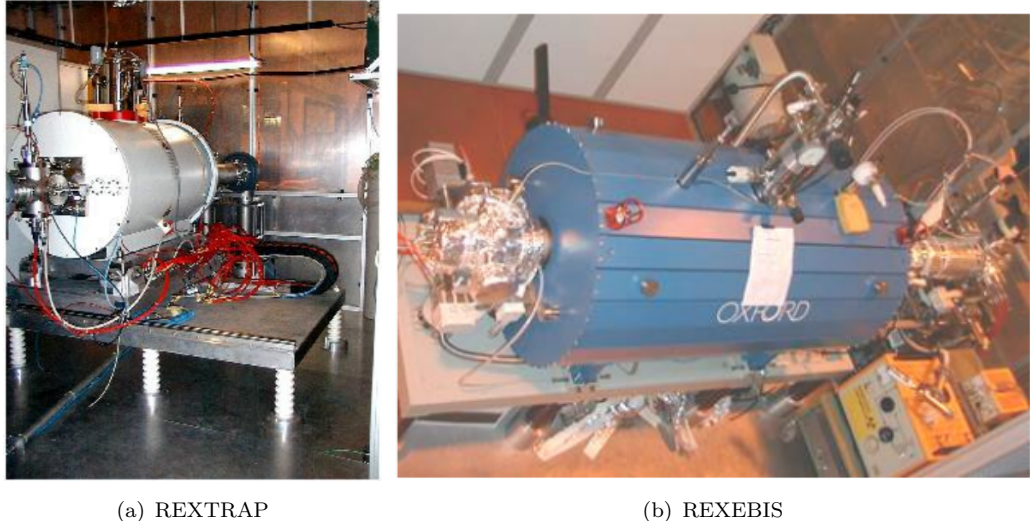


FIGURE 3.5: Images of REXTRAP (left) and REXEBIS (right) at ISOLDE, CERN.

an electron gun (cathode) which is focused by employing a 2 T magnetic field within a superconducting solenoid. The ions are confined within the negative space charge of the electron gun inside the magnetic field and the electric field generated by the electrodes at the front and back side of the EBIS. The breeding time is dependant on the  $A/q$  ratio for the isotope of interest [26]. Following the beams extraction from REXEBIS, it has to be separated with respect to the  $A/q$  ratio since contaminants may outweigh the desired radioactive isotope. Most contaminations are due to residual gas inside REXEBIS. A high vacuum of  $10^{-11}$  mbar is maintained within the EBIS to improve charge breeding as well as to suppress the production of contaminants.

### 3.1.2.3 A/q separator

The mass separator that connects REXEBIS to the REXLINAC is mounted vertically in a S-shaped structure. The selection of the correct  $A/q$  ratio is achieved with the use of a  $90^\circ$  electrostatic deflector which is followed by a  $90^\circ$  magnetic bender. The electrostatic deflector is used to minimise the energy spread from REXEBIS while the magnetic bender selects the correct  $A/q$  and eliminates most of the contaminants. Contaminants with similar energy and similar  $A/q$  will pass the mass separator and reach the final experimental setup. The most expected contamination are carbon, oxygen, nitrogen, neon and argon which are produced in REXTRAP and REXEBIS.

### 3.1.2.4 REXLINAC

The bunched and separated ions are injected into REXLINAC, the compact linear accelerator stationed in the ISOLDE facility. REXLINAC is a room temperature accelerator designed to post-accelerate radioactive ion beams with  $A/q < 4.5$ . REXLINAC is comprised of a radio-frequency quadrupole accelerator (RFQ), an interdigital H structure (IH), three 7-gap resonators and a 9-gap resonator; each of which increases the beam energy in the subsequent steps. Figure 3.6 shows a schematic overview of REXLINAC.

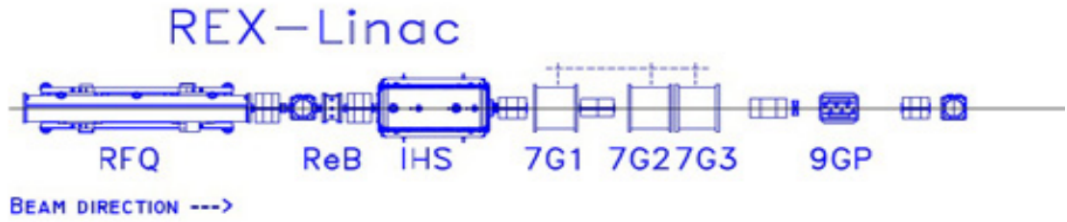


FIGURE 3.6: REXLINAC at ISOLDE, CERN. A breakdown of the components that make up the LINAC are shown. [21]

The ion beams are injected in the RFQ with an energy of 5 keV/u. The RFQ accelerates the beam to 300 keV/u and injects it into the IH structure. The 20-gap IH cavity operates at a frequency of 101.228 MHz and increases the beam energy to 1.2 MeV/u [44]. The subsequent 7-gap resonators operate at the same frequency as the IH structure and allows the beam energy to be tuned in the range of 0.8 to 2.0 MeV/u. The final boost of energy is achieved with 9-gap resonator. This 9-gap IH unit operates at double the frequency of the 7-gap resonators and allows the beam energy to be increased to 3.0 MeV/u. The beam energy may vary between a few 100 to  $10^7$  ions/s, which is measured using Faraday cups, multi-channel plates (MCP) and phosphor screens [26]. At beam intensities below 0.1 pA, the measure devices are not able to detect the beam. For this reason, a stable beam with enough intensity and a similar  $A/q$  ratio is used to obtain the set of accelerator parameters [26].

### 3.1.2.5 HIELINAC

To further increase the science opportunities at ISOLDE, it was evident that a beam energy upgrade was needed. In 2006, it was commissioned to expand the existing REXLINAC with an additional superconducting linear accelerator, high energy beam transfer lines and three additional experimental beam lines [26]. With these upgrades, the superconducting post-accelerator at ISOLDE is known as HIELINAC and consists of six cryomodules with a total of 32 radiofrequency cavities. The upgrade to REXLINAC

happened in three phases. The first phase was designing and installing two of the cryomodules. Each of these cryomodules consists of five high-beta cavities, operating at 101.28 MHz and a superconducting solenoid magnet. Figure 3.7 shows the complete assembly of one of the cryomodules.



FIGURE 3.7: One of the cryomodules being installed in the ISOLDE hall. [7]

The experiment that this work is based on was performed in 2017 after the first phase was completed, which allowed the beam energy to be enhanced to 5.5 MeV/u for nuclei with  $A/q < 4.5$ . The resulting beam energy of the unstable  $^{66}\text{Ge}$  isotope was 4.395 MeV/u with an  $A/q = 4.125$ . The second phase, which was completed in 2018, comprised of installation of an additional cryomodule with similar specification as previously mentioned. The final phase of the upgrade, which is currently taking place is to replace the 7-gap and 9-gap resonator structures from REXLINAC with two more cryomodules. Each of these cryomodules consists of six low-beta cavities and two superconducting solenoid magnets. After the completion of the final phase, HIELINAC will be able to provide radioactive ion beams with energies up to 10.0 MeV/u without the beam quality degrading.

### 3.1.3 Beam Time Structure

The radioactive ion beams at ISOLDE are bunched. To ensure that the beam is delivered in an efficient manner, ISOLDE employs a timing structure. Figure 3.8 illustrates a typical time structure at ISOLDE.

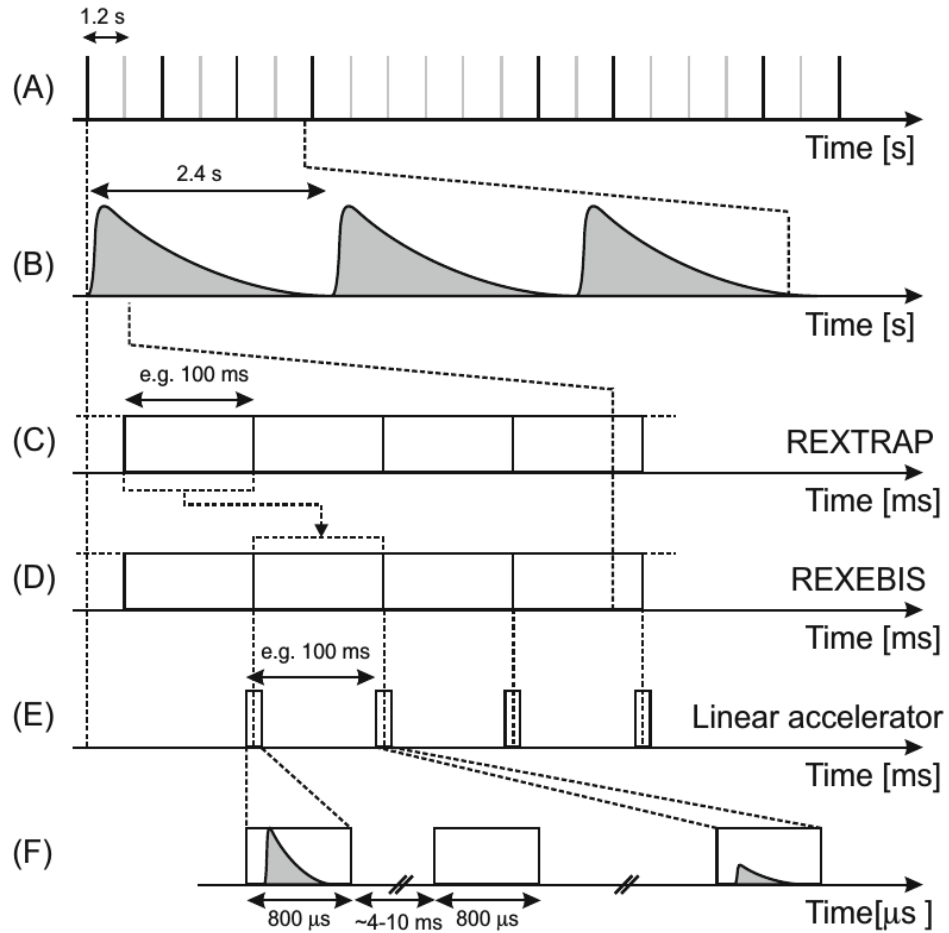


FIGURE 3.8: Time structure for the radioactive ion beam at CERN. See text for more details.

There are many factors which impact the time structure: the time of the delivered proton beam, release characteristic of the target and ion source, decay of the desired radioactive ions and the duty cycle of the bunching, breeding and accelerating devices. Timing signals are used to keep control over the entire sequence from proton impact to beam delivery at the experimental setup. The first signal (A) is available at the beginning of each super-cycle of the PSB. A super-cycle consists of a sequence of a preset number of individual cycles of 1.2 s each. This signal is used as a trigger for a shutter which blocks the laser if laser ionization is used. The second signal (B) is sent when the proton beam makes impact with the ISOLDE primary target. The time difference between this signal and the detection of the beam at the experimental setup can be used to discriminate background or to identify contaminants. This is due to the fact that nuclei have characteristic lifetimes and release times. The third signal (C-D) is sent at the point when the ions are injected from REXEBIS into the REXLINAC. This signal is used to synchronize injection into the REXLINAC which ensure proper

acceleration and transmission (E). This signal also facilitates a 1 ms long "ON beam" window used by the data acquisition system (DAQ) of the MINIBALL detection system (F).

## 3.2 MINIBALL

The MINIBALL array is comprised of 8 triple cluster detectors which are mounted within the MINIBALL frame coupled with a target chamber. Figure 3.9 shows the MINIBALL clusters surrounding the target chamber used in this experiment. The target chamber houses the  $4 \text{ mg/cm}^2$   $^{194}\text{Pt}$  target used in the CE experiment as well as the Double Sided Silicone Strip Detector (DSSSD) used to detect scattered particles.

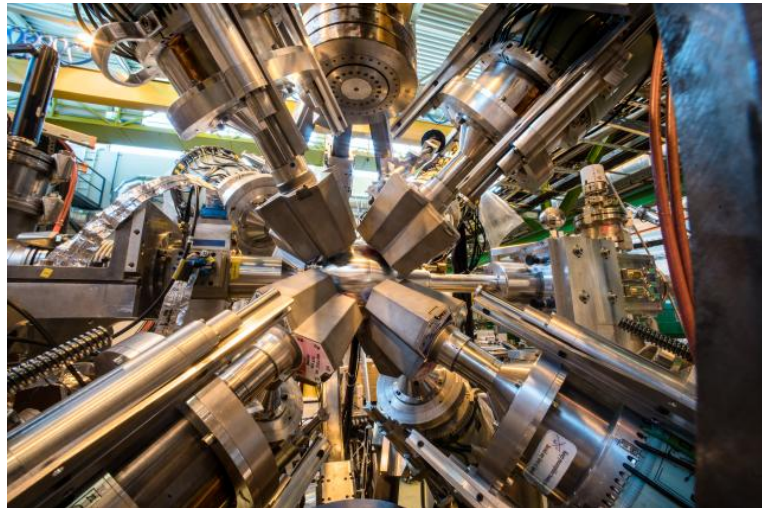


FIGURE 3.9: The target chamber used in the CE of  $^{66}\text{Ge}$  surrounded by the triple cluster germanium detectors. Figure adapted from [37].

The frame was designed to ensure maximum flexibility for positioning of the MINIBALL clusters around the target chamber. The MINIBALL frame was built in two halves which can be slid apart on rails to give access to the target chamber. The clusters are mounted on arms which allow for four degrees of freedom. The clusters are mounted on three toothed arcs which can be rotated about a vertical axis. These mountings are interlocked with the teeth of the arcs, allowing each cluster to be moved up and down in a controlled manner. The cluster mountings also consist of rods that enable the clusters to be moved in and out relative to the target. The clusters can also be rotated around their own axis on the mount. The degrees of freedom are illustrated in Figure 3.10.

Section 3.2.1 discusses the high-purity germanium detectors used for detecting  $\gamma$ -rays. Section 3.2.2 details the particle detector used to detect scattered particles. Section

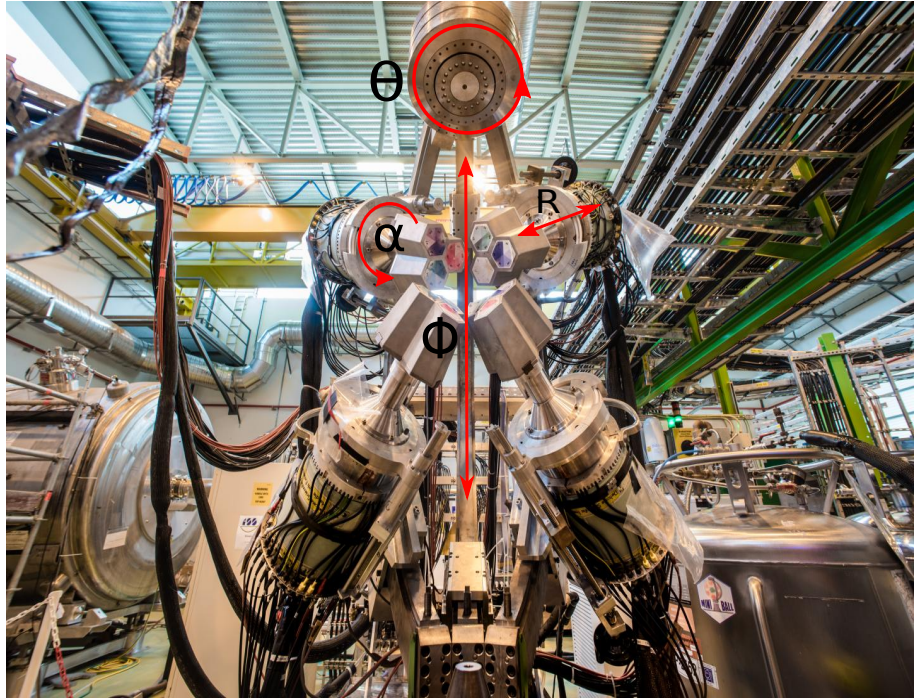


FIGURE 3.10: Four triple clusters mounted on the one half of the MINIBALL frame. The four degrees of freedom are marked. Figure adapted from [37].

3.2.3 expands on the data acquisition system used to process the data collected during the experiment.

### 3.2.1 High-Purity Germanium Detectors

The development of high-purity germanium (HPGe) detectors has allowed tremendous advances in nuclear physics and other fields. Germanium is an intrinsic semiconductor, and can be made n- or p-type with the introduction of donor (lithium) or acceptor (boron) impurities. The removal of impurities allows the germanium to be almost completely depleted of charge carriers to allow large charge-sensitive regions to be created. Each triple cluster contains three individually encapsulated six-fold segmented HPGe crystals. The germanium crystals are 78 mm long and have a diameter of 70 mm. The left panel of Figure 3.11 shows one of the triple cluster detectors. A total of 144 individual segment signals and an additional 24 signals from the central electrodes are measured. The high granularity of the system reduces the opening angle of the detection and, therefore, enhances the position sensitivity [46]. This sensitivity to the interaction point is used to correct for Doppler shift of the detected  $\gamma$ -rays. The energy resolution of the MINIBALL spectrometer after addback, measured with a  $^{60}\text{Co}$  source, amounts to 2-3 keV at 1.332 MeV. This good energy resolution is achieved by operating the detector system at liquid nitrogen temperature. The signals from the detector system is

processed using XIA digital gamma finders to enable high count rates and allows for proper event building [46].

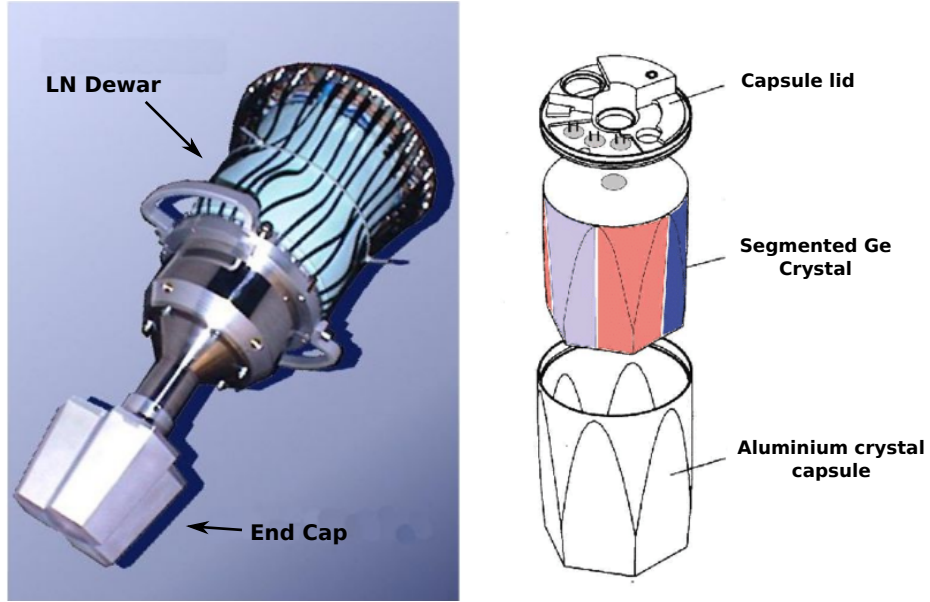


FIGURE 3.11: Left: A single MINIBALL triple cluster connect to the liquid nitrogen dewar for cooling purposes. Right: Exploded view of one of the segmented germanium crystals.

### 3.2.2 Particle Detector

The angle of emission of the  $\gamma$ -ray needs to be combined with the momentum vector of the deexciting emitting particle to perform Doppler correction. To measure the ion energy and position, a Double-Sided Silicone Strip Detector (DSSSD) was employed along with the 8 triple clusters. The DSSSD is composed out of four identical quadrants that make up the CD-like structure. Figure 3.12 illustrates both sides of the DSSSD.

The thickness of each quadrant is  $138 \mu m$  with a typical dead layer of  $200 \text{ nm}$  sufficient enough to stop heavy ion beams. The DSSSD has an inner diameter of  $9 \text{ mm}$  and an outer diameter of  $40.9 \text{ mm}$ . The front side is divided into 16 annular strips ( $p+n$  junction) and the back side is divided into 24 radial strips ( $n+n$  ohmic). The 16 rings on the front side have a pitch of  $2.0 \text{ mm}$ , while the 24 sectors on the back are arranged in  $3.5^\circ$  sectors with a  $3.6^\circ$  opening angle [38]. The 24 strips have been shorted allowing 2 consecutive strips to operate as 1 and thus resulting in 12 strips on the back. The azimuthal symmetry of the DSSSD allows for a simple relation with scattering angle, while the high granularity aids in the angular correlation to coincident  $\gamma$ -rays allowing for a well determined Doppler correction. The DSSSD was placed  $27.34 \text{ mm}$  downstream from the target with respect to the incoming beam and covered forward scattering angles

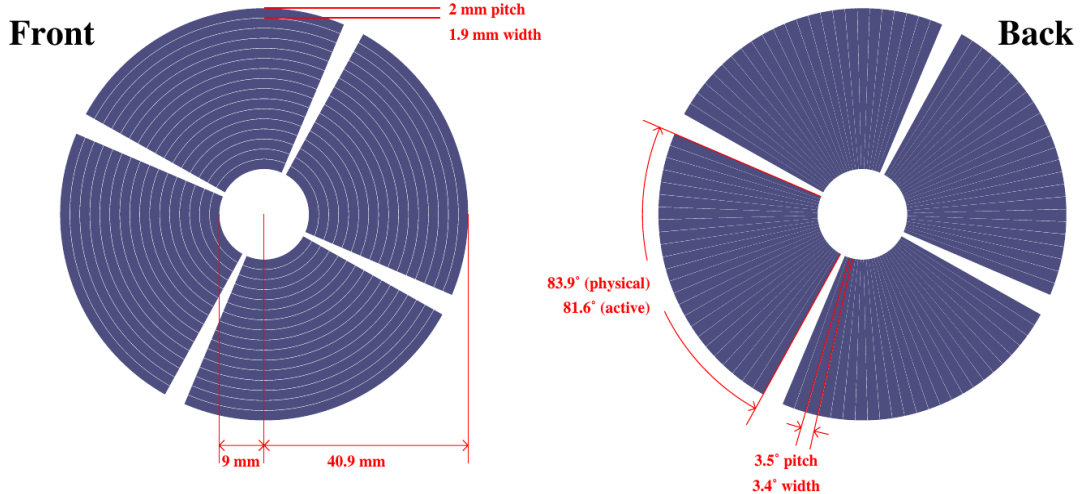


FIGURE 3.12: Schematic drawing of the double-sided strip detector. The front side has 0.1 mm, inactive regions between the rings and the back side consists of  $0.1^\circ$  inactive regions between the strips.

between  $19^\circ$  to  $56^\circ$  in the laboratory frame. Figure 3.13 shows the DSSSD mounted in the target chamber.



FIGURE 3.13: Picture of the DSSSD mounted in the target chamber. The 16 annular rings can be seen [37].

### 3.2.3 Data Acquisition

The data acquisition system (DAQ) used to record events during the CE experiment is responsible for the collection and sorting of data. The DAQ is made up of both hardware and software elements. The hardware elements consists of Digital Gamma Finders 4C (DGF-4C), Mesytec 32 channel multiplexers (MUX-32) and peak sensing

Analog-to-Digital Converters (ADC) used to collect the data from both the  $\gamma$ -rays as well as particles. The software element of the DAQ is called MARABOU [32] (find out how to correct make this name in latex), which consists of the front end of Multi Branch System (MBS) read out, developed at GSI, Darmstadt, and the backend framework ROOT. The data processing of MARABOU is illustrated in Figure 3.14.

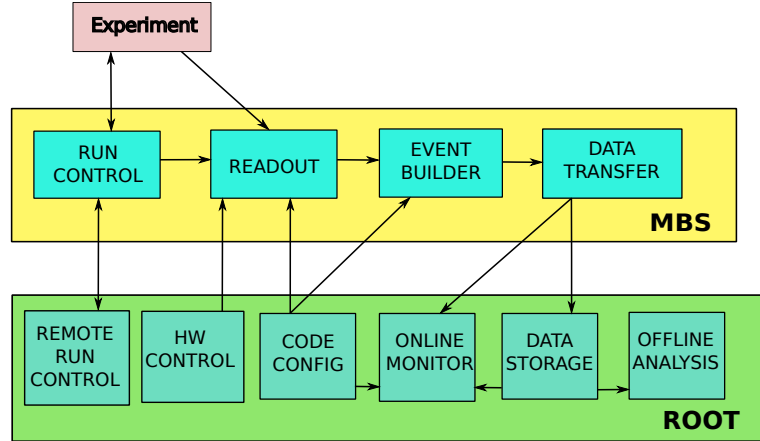


FIGURE 3.14: Schematic illustration of the data processing of MARABOU. [32].

The MBS front end facilitates the data readout, event building and data transfer, whereas ROOT provides an environment to do setup configuration, run and hardware control, online/offline data visualization using histograms, data analysis and data storage. The following tasks were handled by the DAQ during the experiment:

- Recording of the experimental data,
- Conversion of MBS events into ROOT trees,
- Assign energy, position and timing information for each event,
- Online and offline visualization of the physical data, and
- Store the event data into ROOT format for further post-processing.

## Chapter 4

# Data Analysis and Results

This chapter gives details about the calibration of the equipment used to record the data as well as post-processing of the data to determine the spectroscopic quadrupole moment for  $^{66}\text{Ge}$ . The chapter starts by describing the detector calibration for both the DSSSD and HPGe triple cluster detectors in Section 4.1. Section 4.2 discusses Doppler correction which is followed by details on particle- $\gamma$  coincidence in Section 4.3. The chapter concludeds with a discussion on the determination of the beam composition for the investigated beam produced at the ISOLDE facility in Section 4.4.

### 4.1 Detector Calibration

To accurately determine the spectroscopic quadrupole moment from the data, both the DSSSD as well as the HPGe triple clusters need to be calibrated. Energy and efficiency calibrations for the HPGe crystals are performed using well known calibration sources whereas the DSSSD is calibrated using in-beam data since an alpha source does not sufficiently cover the energy range of the beam. The following sections discusses each of these in more detail.

#### 4.1.1 HPGe Cluster Calibration

The calibration for the HPGe cluster crystals was performed using a combination of two calibration sources, namely  $^{152}\text{Eu}$  and  $^{133}\text{Ba}$ . The  $^{133}\text{Ba}$  source provides low energy  $\gamma$ -rays ranging from 80 keV to about 400 keV whereas  $^{152}\text{Eu}$  provides  $\gamma$ -rays transitions ranging from 122 keV up to 1.5 MeV. These proves sufficient to obtain an accurate calibration for the first  $2^+$  transition of  $^{66}\text{Ge}$  at 956 keV. The two sources were mounted at the target position ensuring all the crystals of MINIBALLS could detect the  $\gamma$ -rays

being emitted. The energy calibration using the  $^{152}\text{Eu}$  transitions only was found to be sufficient as it already provided lower energy  $\gamma$ -rays. The recorded  $\gamma$ -ray spectrum is shown in Figure 4.1.

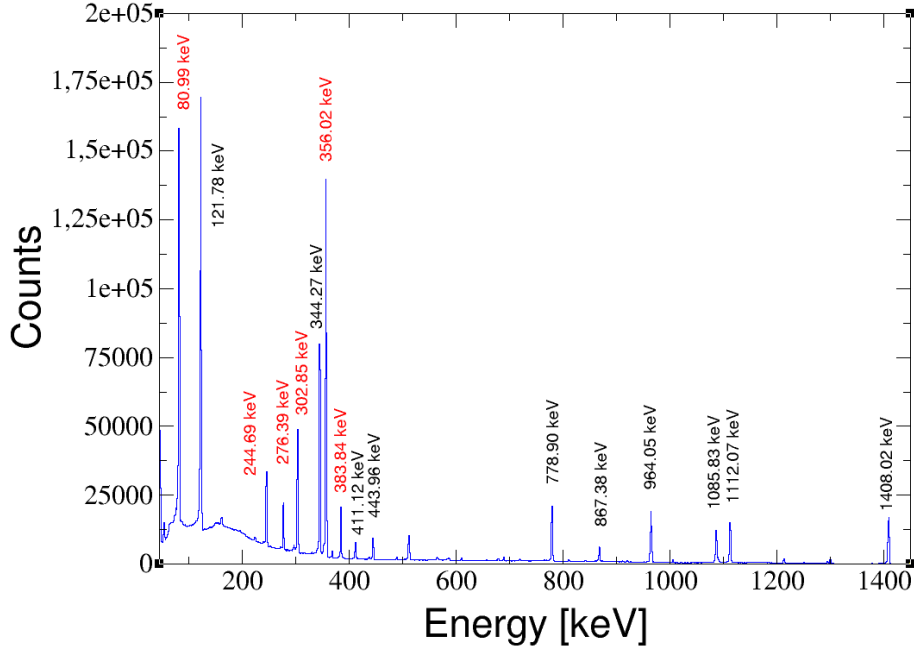


FIGURE 4.1: A spectrum of the  $^{152}\text{Eu}$  and  $^{133}\text{Ba}$  calibration sources used to calibrate the clover detectors. Peaks with red labels belong to  $^{133}\text{Ba}$  and the those with black labels belong to  $^{152}\text{Eu}$ .

A total of 16 dominant transitions were identified and are shown labelled in Figure 4.1. The energy calibration was performed for each of the 24 detectors of MINIBALL by fitting the 16 transitions in the core spectrum. A linear fit was performed to determine the calibration coefficients for that crystal. A fit for a single core along with the gain and offset obtained are presented in Figure 4.2.

In addition to the energy calibration, an efficiency calibration was also performed using the  $^{152}\text{Eu}$  source. The efficiency fit was performed using the GF3 program that forms part of the RADware package [40]. GF3 takes as input the centroids, peak areas and peak energies as well as the errors of each of the strong transitions of  $^{152}\text{Eu}$  and calculates its relative intensities before saving it to file. This new input file is used with EFFIT, another program in the RADware package, to obtain the efficiency curve. EFFIT fits this data using the following expression:

$$\ln(\epsilon) = [\epsilon_l + \epsilon_h]^{-\frac{1}{G}}, \quad (4.1)$$

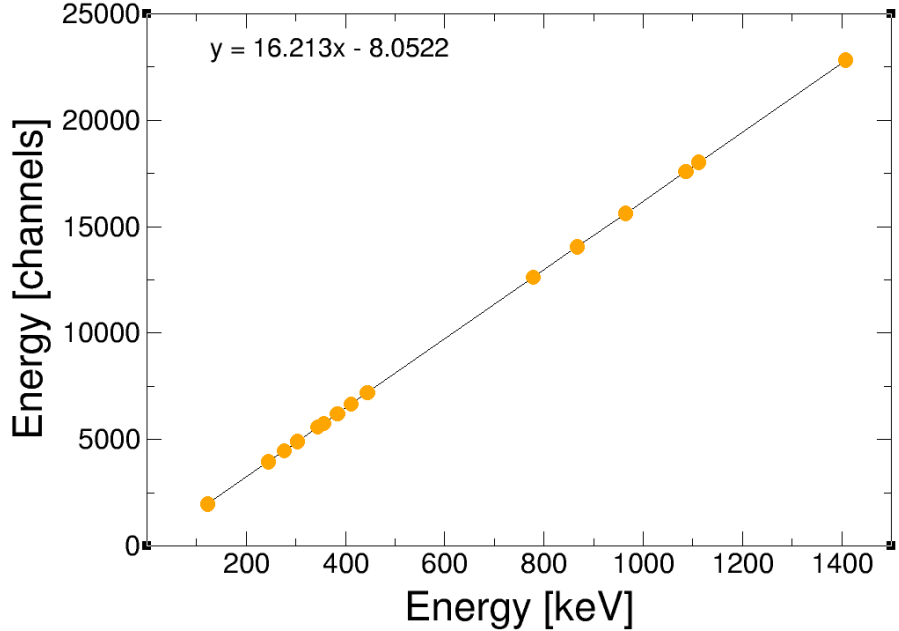


FIGURE 4.2: A fit to the  $^{152}\text{Eu}$  data for one of the core of a clover detector. The gain and offset are given in the equation of the linear fit.

where  $\epsilon_l$  and  $\epsilon_h$  denote the efficiencies of the low and high energy regions, respectively, and  $G$  is the interaction parameter between the two regions. The lower region  $\epsilon_l$  is calculated as follows:

$$\epsilon_l = (A + Bx + Cx^2)^{-G}, \quad (4.2)$$

where  $A$ ,  $B$  and  $C$  are the fitting parameters for the lower region of the  $\gamma$ -ray spectrum and  $x = \log(\frac{E_\gamma}{E_1})$  with  $E_1 = 100$  keV. Similarly, the higher region is calculated using:

$$\epsilon_h = (D + Ey + Fy^2)^{-G}, \quad (4.3)$$

where  $D$ ,  $E$  and  $F$  are the fitting parameters for the higher region and  $y = \log(\frac{E_\gamma}{E_2})$  with  $E_2 = 1$  MeV. The resulting efficiency curve and the fitting parameter values for EFFIT are shown in Figure 4.3.

#### 4.1.2 DSSSD Energy Calibration

As aforementioned, the DSSSD is made up of four identical quadrants with 16 annular segments on the front side and 12 strips, perpendicular to the rings on the back side. This results in 1024 individual pixels which are used to detect the scattering particles

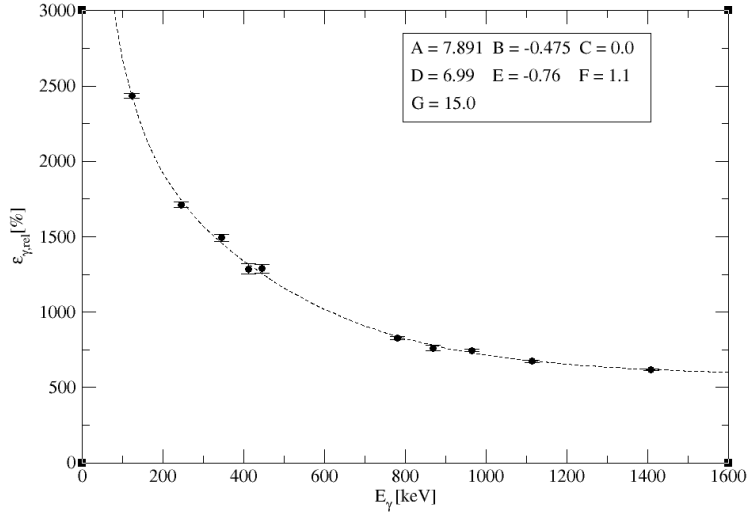


FIGURE 4.3: The kinematics obtained with LISE++ for  $^{16}\text{O}$  onto  $^{196}\text{Pt}$  as a function of scattering angle. The dashed lines represents the angles that the different rings cover in the lab frame.

with high position sensitivity. Each hit on a ring is recorded with a corresponding hit on a sector. Events on the front side of the DSSSD are subjected to energy shifts due to the kinematics and energy losses through the target, while events on the back side are recorded at the same energy. The beam energy amounts to 290 MeV in the laboratory frame thus making a calibration with a typical alpha source insufficient due to large deviations resulting from extrapolation. The DSSSD was therefore calibrated using a cocktail beam, consisting of  $^{12}\text{C}$ ,  $^{16}\text{O}$ ,  $^{20}\text{Ne}$  and  $^{40}\text{Ar}$ , mass separated using  $A/q = 4$  and bombarded onto a  $^{196}\text{Pt}$ . The  $^{196}\text{Pt}$  target had a thickness of  $1.4 \text{ mg/cm}^2$  and the beam energy was 5.54 MeV/u. For each of the nuclei in the cocktail beam, a kinematics calculation was done using the simulation program LISE++ [3]. LISE++ calculates the energy of the scattering nucleus after a scattering event with the target in question as well as the energy of the recoil for each ring in the DSSSD. The in-beam data for the cocktail beam give the channel number for the peaks of interest for each ring and, thus, a calibration can be done. Figure 4.4 illustrates the kinematics for  $^{16}\text{O}$  as it interacts with the  $^{196}\text{Pt}$  target.

The calibrated spectra each quadrant is shown in Figure 4.5, where an overlap of the peaks are seen at 240 MeV.

## 4.2 Doppler Correction

When performing CE experiments using high energy beams, the  $\gamma$ -ray energies have to be corrected due to the Doppler effect. For this experiment, a recoil velocity of  $\beta \sim 10\%$

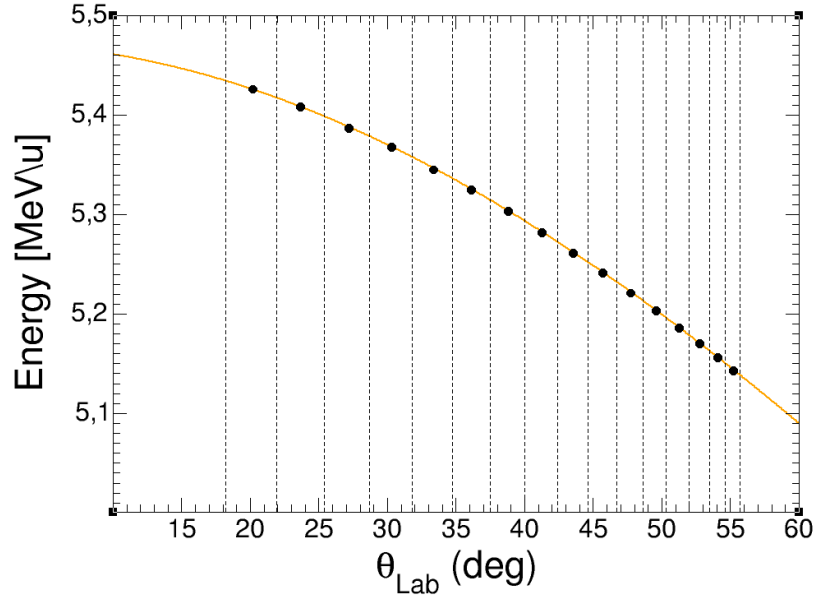


FIGURE 4.4: The kinematics obtained with LISE++ for  $^{16}\text{O}$  onto  $^{196}\text{Pt}$  as a function of scattering angle. The dashed line represents the angles that the different rings cover in the lab frame.

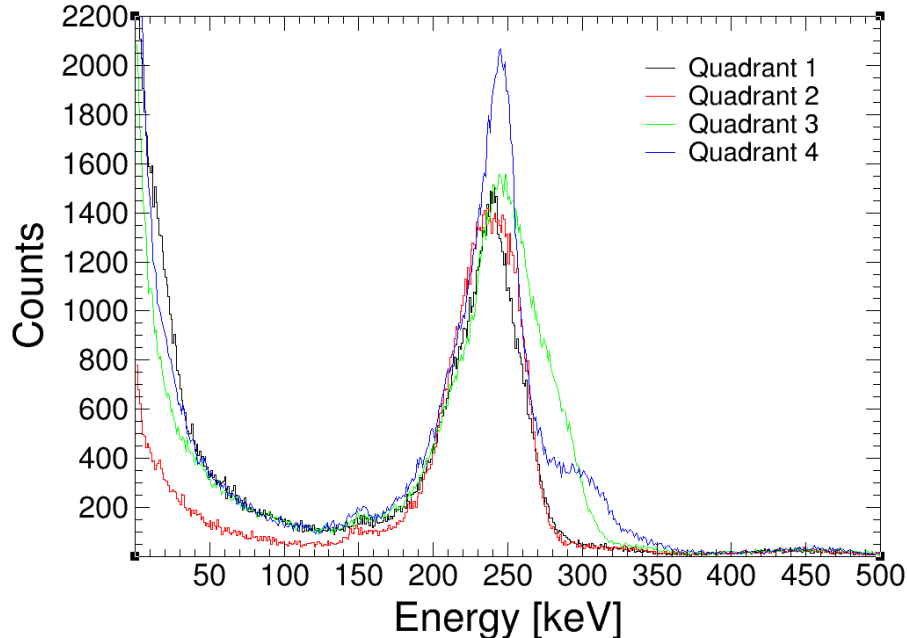


FIGURE 4.5: The kinematics obtained with LISE++ for  $^{16}\text{O}$  onto  $^{196}\text{Pt}$  as a function of scattering angle. The dashed line represents the angles that the different rings cover in the lab frame.

is observed. The  $\gamma$ -rays are detected with a large Doppler broadening due to the high recoil velocity and the close configuration of the HPGe detectors of MINIBALL. The interaction position of the  $\gamma$ -ray inside the HPGe crystals and the particle position within

the DSSSD have to be known precisely to perform a proper correction. The correction of the  $\gamma$ -ray energies are given by:

$$E_{\gamma,0} = \frac{E_{\gamma,lab}(1 + \beta \cos(\theta_{p\gamma}))}{\sqrt{1 - \beta^2}}, \quad (4.4)$$

where  $E_{\gamma,lab}$  is the energy measured in the laboratory frame,  $E_{\gamma,0}$  is the energy of the emitted  $\gamma$ -ray in the rest frame and  $\theta_{p\gamma}$  is the angle between the particle momentum vector and the direction of the emitted  $\gamma$ -ray with

$$\cos(\theta_{p\gamma}) = \sin(\theta_{lab,\gamma}) \sin(\theta_{lab,\gamma}) \cos(\phi_{lab,p} - \phi_{lab,\gamma}) + \cos(\theta_{lab,\gamma}) \cos(\theta_{lab,p}). \quad (4.5)$$

The detected observables  $\theta_{lab,\gamma}$  and  $\phi_{lab,\gamma}$  are the detected angles of the MINIBALL crystals and  $\theta_{lab,p}$  and  $\phi_{lab,p}$  are the detected angles of the DSSSD detectors. A high position sensitivity is achieved with MINIBALL using the granularity of the six-fold segmented triple clusters which ensures an improved assignment of the interaction position within each HPGe.

In order to use the position sensitivity of MINIBALL, a position calibration measurement needed to be performed. An independent stable experiment was performed with a  $^{22}\text{Ne}$  beam which employs  $d(^{22}\text{Ne}, ^{23}\text{Ne})p$  and  $d(^{22}\text{Ne}, ^{23}\text{Na})n$  transfer reactions. The approach is as follows:

1. The position of each triple cluster can be described by a set of four parameters  $R_i$ ,  $\phi_i$ ,  $\theta_i$  and  $\alpha_i$  as illustrated in Figure 4.6.
2. After the transfer reactions, the excited  $^{22}\text{Ne}$  and  $^{23}\text{Na}$  decay in flight by emitting  $\gamma$ -rays which are recorded in the HPGe detectors with a Doppler broadening. From the kinematics of the reaction, the scattering angles of the recoiling nuclei are small and negligible, thus, the energy shift depends solely on the position where the  $\gamma$ -ray was detected. For each segment, a set of the aforementioned parameters are determined to correct the  $\gamma$ -rays according to Equation 4.4.
3. To help facilitate this process, an algorithm which implements neural networks, written in ROOT by Nigel Warr was used. This algorithm uses the doppler shifted 440 keV  $\gamma$ -ray of the  $d(^{22}\text{Ne}, ^{23}\text{Na})n$  reaction and minimizes the set of four parameters. These parameters are then used to compare the calculated  $\gamma$ -ray energies with the measured ones. A  $\chi^2$  minimization fit is employed for this purpose.

The resulting parameter sets for each core is used to perform the final doppler correction of the  $^{66}\text{Ge}$  data. TABLE 4.1 shows the results of the genetic algorithm.

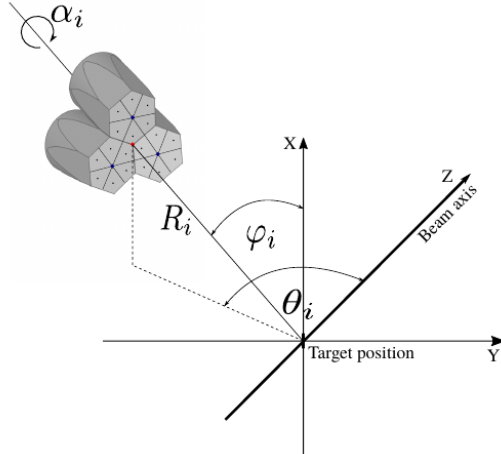


FIGURE 4.6: The parameters used to calibrate the position of each triple cluster with respect to the beam line.

TABLE 4.1: Position parameters used for the center of each MINIBALL triple cluster for the Doppler correction

MB Cluster	$R_i$ [mm]	$\theta_i$ [ $^\circ$ ]	$\phi_i$ [ $^\circ$ ]	$\alpha_i$ [ $^\circ$ ]
MB17	97.81	144.57	132.42	321.65
MB12	94.21	49.36	63.11	47.89
MB16	97.90	46.34	134.46	52.68
MB13	99.61	144.24	54.81	48.04
MB22	98.41	134.41	231.89	73.58
MB18	95.50	41.70	234.98	110.35
MB14	96.99	131.14	299.72	267.32
MB23	93.77	36.32	260.92	260.92

### 4.3 Particle- $\gamma$ Coincidence

Due to the vast number of  $\gamma$ -rays resulting from radioactive ion beam experiments, it is necessary to employ a particle- $\gamma$  coincidence condition. This is especially important for Coulomb Excitation experiments with radioactive ion beams, as the rare  $\gamma$ -ray transition of interest may be hidden behind background. This background could result from the  $\beta$ -decay of the radioactive ions implanted in the target chamber and along the beam line as well as bremsstrahlung from the accelerator. Figure 4.7 illustrates a raw  $\gamma$ -ray singles spectra with the energy of the first  $2^+$  transition of  $^{66}\text{Ge}$  marked. As can be seen, the transition of interest cannot be identified.

The particle- $\gamma$  condition was set up by requiring a single detection in one of the HPGe cluster segments followed by a hit in both a ring and a sector of the DSSSD within an acceptance time window. The particle- $\gamma$  condition also improves the peak-to-background ratio as any  $\gamma$ -ray detected outside of the acceptance window are subtracted from the

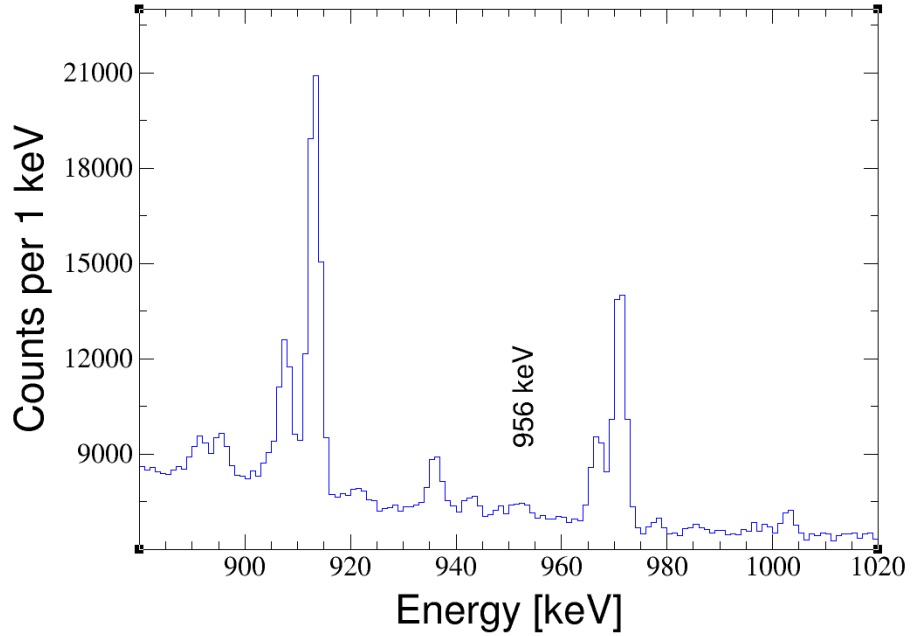


FIGURE 4.7: A  $\gamma$ -ray singles spectrum for  $^{66}\text{Ge}$  on  $^{196}\text{Pt}$  with no particle- $\gamma$  coincidence conditions applied. The energy of the first  $2^+$  transition at 956 keV is marked.

resulting particle spectra. Only prompt  $\gamma$ -rays which are detected within a  $\Delta t_p = 160$  ns time window relative to the particle in the DSSSD are selected for the final  $\gamma$ -ray spectra. A time window for the random  $\gamma$ -rays,  $\Delta t_r$ , is also selected such that background can be determined and subtracted from the final  $\gamma$ -ray spectra. Figure 4.8 shows the time difference acceptance windows for prompt and random  $\gamma$ -rays used to generate the final particle- $\gamma$  coincidences.

The resulting  $\gamma$ -ray spectra from the prompt window gated on beam particles are shown in Figure 4.9. It should be noted that this spectra is not Doppler corrected.

The random  $\gamma$ -ray spectra is subtracted from the resulting prompt spectra and Doppler correction is applied. The final  $\gamma$ -ray spectra is particularly clean from backgroud radiation and mostly contains transitions caused by CE. Figure 4.10 shows the beam gated background subtracted spectra for the  $^{196}\text{Pt}$  target. Figure 4.11 shows the final beam gated background subtracted spectra after applying Doppler correction, where the first  $2^+$  transition of  $^{66}\text{Ge}$  at 956 keV can be clearly seen.

## 4.4 Beam Composition

As previously mentioned in Section 3.1.1, the final beam used for the experiment contained traces of both  $^{66}\text{Ge}$  and  $^{70}\text{Se}$ . To determine an accurate spectroscopic quadrupole

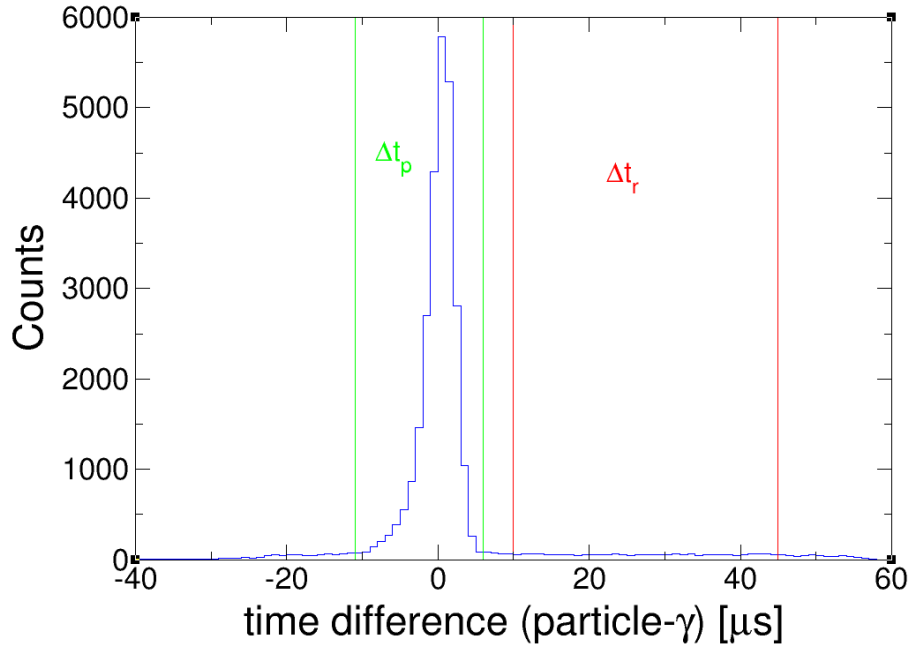


FIGURE 4.8: Time difference between the clover detectors and the DSSSD. Prompt and random time windows are marked, which are used to generate the final  $\gamma$ -ray spectra.

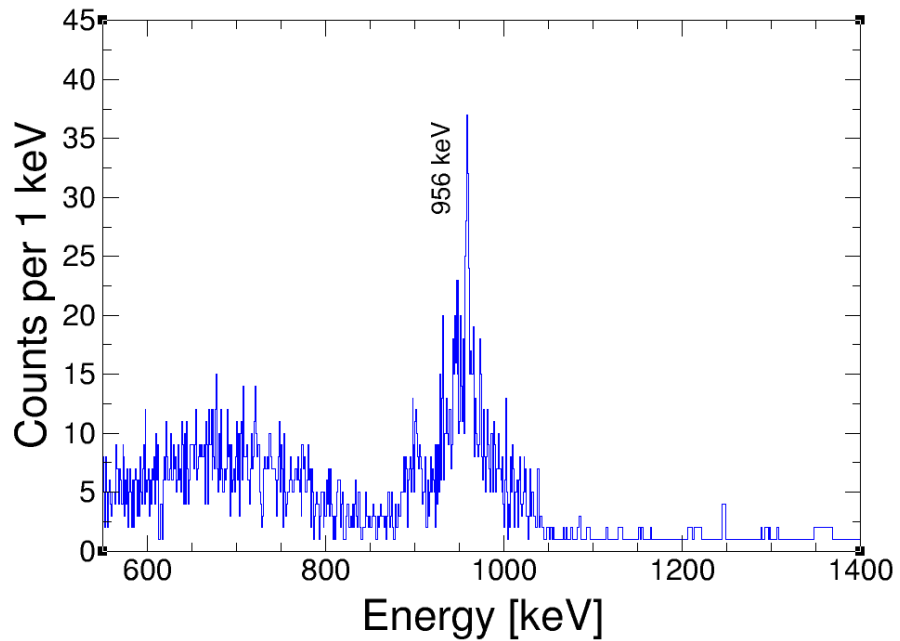


FIGURE 4.9: The resulting  $\gamma$ -ray spectrum from the prompt time window. The range of this spectrum was decreased to not include the 511 keV transition such that the first  $2^+$  state in  $^{66}\text{Ge}$  can be seen.

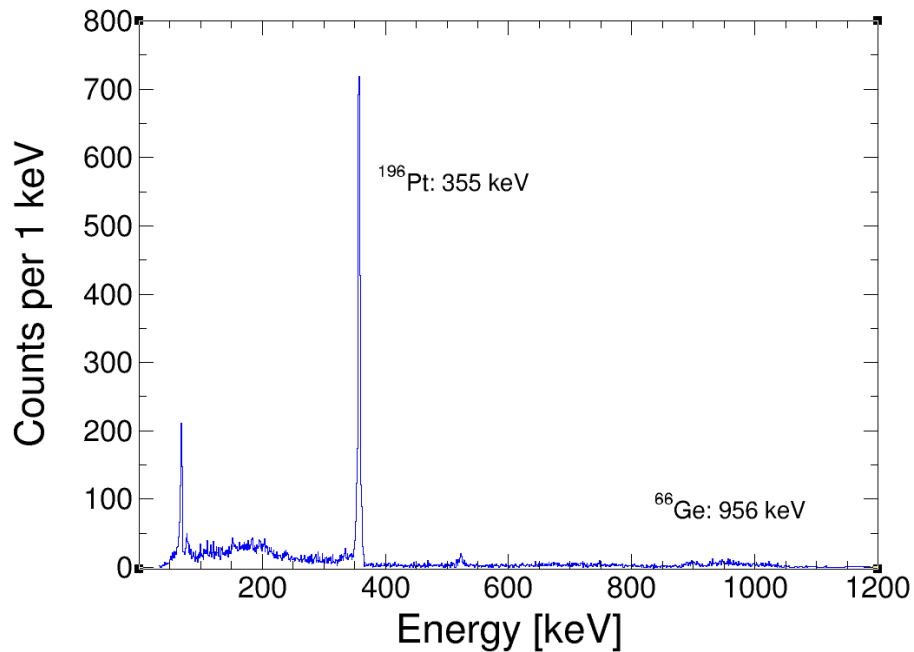


FIGURE 4.10: The resulting beam gated  $\gamma$ -ray spectrum after background subtraction.  
The first  $2^+$  state in  $^{196}\text{Pt}$  is marked.

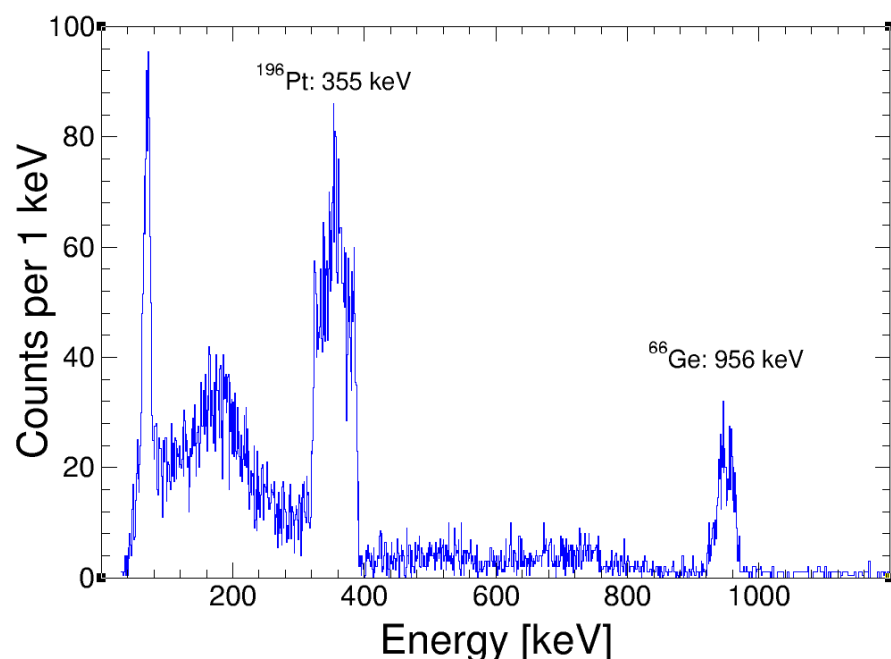


FIGURE 4.11: The resulting  $\gamma$ -ray spectrum after Doppler correction and background subtraction. The first  $2^+$  state in  $^{66}\text{Ge}$  can clearly be seen.

moment for  $^{66}\text{Ge}$ , the ratio of selenium to germanium needs to be known precisely. As shown in Figure 4.12, potential beam contaminants are possible along the isobaric chains  $A = 66$  as well as  $A = 70$  since the mass separators are only selective to mass-over-charge ratio.

$^{68}\text{Se}$ $\beta^+$	$^{69}\text{Se}$ $\beta^+$	$^{70}\text{Se}$ $\beta^+$	$^{71}\text{Se}$ $\beta^+$	$^{72}\text{Se}$ e- capture
$^{67}\text{As}$ $\beta^+$	$^{68}\text{As}$ $\beta^+$	$^{69}\text{As}$ $\beta^+$	$^{70}\text{As}$ $\beta^+$	$^{71}\text{As}$ $\beta^+$
$^{66}\text{Ge}$ $\beta^+$	$^{67}\text{Ge}$ $\beta^+$	$^{68}\text{Ge}$ e- capture	$^{69}\text{Ge}$ $\beta^+$	$^{70}\text{Ge}$ Stable
$^{65}\text{Ga}$ $\beta^+$	$^{66}\text{Ga}$ $\beta^+$	$^{67}\text{Ga}$ e- capture	$^{68}\text{Ga}$ $\beta^+$	$^{69}\text{Ga}$ Stable
$^{64}\text{Zn}$ Stable	$^{65}\text{Zn}$ $\beta^+$	$^{66}\text{Zn}$ Stable	$^{67}\text{Zn}$ Stable	$^{68}\text{Zn}$ Stable

FIGURE 4.12: Nuclei along the isobaric chains  $A = 66$  and  $A = 70$  that could potentially contribute to the beam composition are marked with red squares.

The primary ISOLDE beam is extracted as a singly-charged molecule beam. In this case,  $^{66}\text{Ge}^{32}\text{S}$  molecules and  $^{70}\text{Se}^{12}\text{C}^{16}\text{O}$  molecules were produced resulting in possible contaminants from ions with  $A = 98$ . The transport from REXTRAP to REXEBIS is managed by an electrostatic steerer and, therefore, no  $A/q$  separation is possible at that stage. Mass  $A = 66$  ions were charge bred in REXEBIS and extracted with charge state  $q = 16^+$ , which results in an  $A/q = 4.125$ . Mass  $A = 70$  ions were charge bred and extracted with charge state  $q = 17^+$  resulting in an  $A/q = 4.118$ . An ionization chamber was setup before the experiment to estimate the target thickness as well as the beam composition. The ionization chamber however was not biased properly and thus could not be used. A  $\beta$ -decay study of the beam had to be performed to determine the beam composition.

#### 4.4.1 $\beta$ -decay investigation

After the experiment, an aluminium stopper foil was placed in the target wheel and bombarded with the beam for 5.5 hours and left to decay for 2 hours. The first step to determining the beam composition is to identify the transition lines of the  $\beta$ -decay spectrum. Figure 4.13 shows the recorded single spectrum when bombarding the beam onto the stopper foil. The observed transitions energies and the corresponding  $\beta$ -decays are listed in Table 2. The majority of the observed transitions are known lines from the decays of  $^{66}\text{Ge} \rightarrow ^{66}\text{Ga}$ ,  $^{66}\text{Ga} \rightarrow ^{66}\text{Zn}$ ,  $^{70}\text{Se} \rightarrow ^{70}\text{As}$ , and  $^{70}\text{As} \rightarrow ^{70}\text{Ge}$ .

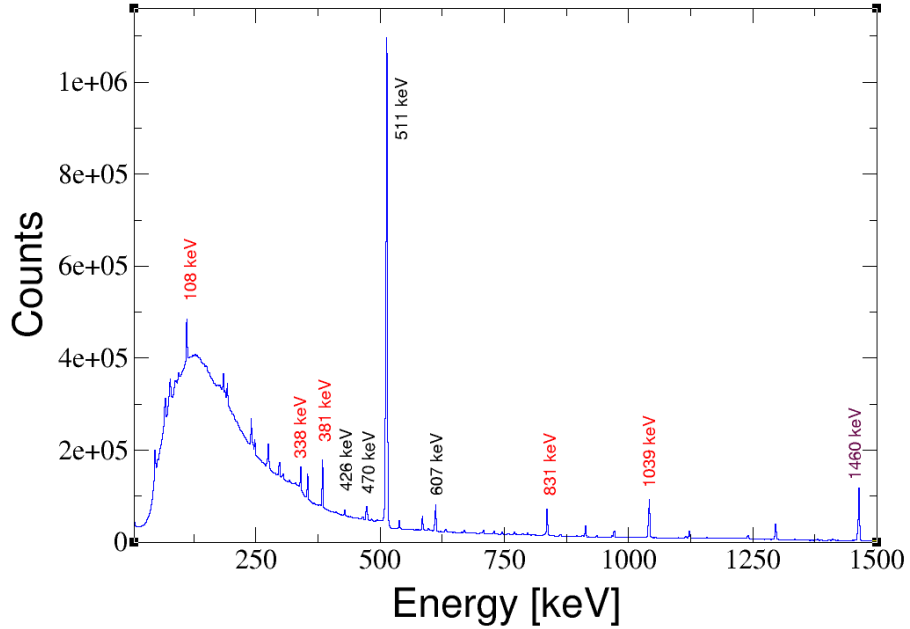


FIGURE 4.13: The resulting  $\beta$ -decay spectrum when bombarding the beam onto an aluminium stopper foil in logarithmic scale.  $\gamma$ -ray transitions with energies up to 3.5 MeV are observed.

The fact that lines from the potassium decay  $^{40}\text{K} \rightarrow ^{40}\text{Ar}$  are observed indicates that transitions with intensities down to the natural background radiation are also identified. In addition, no transitions corresponding to the decay of mass  $A = 98$  ions were observed. In order to deduce how much of the target excitation was induced by  $^{66}\text{Ge}$ , the amount of  $^{70}\text{Se}$  relative to  $^{66}\text{Ge}$  needs to be determined. This is required for the proper normalization of the measured transition strength. The measured intensity of a transition,  $N_\gamma$  is given by:

$$N_\gamma = \frac{A_\gamma}{\epsilon_\gamma I_\gamma}, \quad (4.6)$$

where  $A_\gamma$  is the area of a peak in a  $\gamma$ -singles spectra,  $\epsilon_\gamma$  is the detection efficiency at the energy of the transition and  $I_\gamma$  is the published intensity of the transition. For the determination of the  $\beta$ -decay ratio, the dominant transitions at 381.85 keV ( $^{66}\text{Ge} \rightarrow ^{66}\text{Ga}$ ) and 426.15 keV ( $^{70}\text{Se} \rightarrow ^{70}\text{As}$ ) were used. The  $^{66}\text{Ga}$  transition at 381.85 keV from the  $\beta$ -decay of  $^{66}\text{Ge}$  has an intensity of 28% [12]. Since this transition intensity was published without uncertainty, the maximum uncertainty reported of 0.8% is assumed. The  $^{70}\text{As}$  transition at 426.15 keV from the  $\beta$ -decay of  $^{70}\text{Se}$  has an intensity of 29% [12]. Since this transition intensity was published without uncertainty, the maximum uncertainty reported of 0.6% is assumed. The detection efficiency is determined from

TABLE 4.2: Observed  $\gamma$ -ray transition energies following the corresponding  $\beta$ -decay.

$E_\gamma$ [keV]	$\beta$ -decay	$E_\gamma$ [keV]	$\beta$ -decay	$E_\gamma$ [keV]	$\beta$ -decay
44	$^{66}\text{Ge} \rightarrow ^{66}\text{Ga}$	743	$^{70}\text{As} \rightarrow ^{70}\text{Ge}$	1508	$^{66}\text{Ga} \rightarrow ^{66}\text{Zn}$
65	$^{66}\text{Ge} \rightarrow ^{66}\text{Ga}$	757	$^{66}\text{Ge} \rightarrow ^{66}\text{Ga}$	1522	$^{70}\text{As} \rightarrow ^{70}\text{Ge}$
108	$^{66}\text{Ge} \rightarrow ^{66}\text{Ga}$	796	$^{66}\text{Ga} \rightarrow ^{66}\text{Zn}$	1539	$^{70}\text{As} \rightarrow ^{70}\text{Ge}$
182	$^{66}\text{Ge} \rightarrow ^{66}\text{Ga}$	833	$^{66}\text{Ga} \rightarrow ^{66}\text{Zn}$	1587	$^{70}\text{As} \rightarrow ^{70}\text{Ge}$
190	$^{66}\text{Ge} \rightarrow ^{66}\text{Ga}$	858	$^{70}\text{Se} \rightarrow ^{70}\text{As}$	1707	$^{70}\text{As} \rightarrow ^{70}\text{Ge}$
244	$^{70}\text{Se} \rightarrow ^{70}\text{As}$	893	$^{70}\text{As} \rightarrow ^{70}\text{Ge}$	1780	$^{70}\text{As} \rightarrow ^{70}\text{Ge}$
272	$^{66}\text{Ge} \rightarrow ^{66}\text{Ga}$	906	$^{70}\text{As} \rightarrow ^{70}\text{Ge}$	1872	$^{66}\text{Ga} \rightarrow ^{66}\text{Zn}$
293	$^{70}\text{Se} \rightarrow ^{70}\text{As}$	935	$^{66}\text{Ge} \rightarrow ^{66}\text{Ga}$	1898	$^{66}\text{Ga} \rightarrow ^{66}\text{Zn}$
302	$^{66}\text{Ge} \rightarrow ^{66}\text{Ga}$	963	$^{66}\text{Ga} \rightarrow ^{66}\text{Zn}$	1918	$^{66}\text{Ga} \rightarrow ^{66}\text{Zn}$
338	$^{66}\text{Ge} \rightarrow ^{66}\text{Ga}$	1039	$^{66}\text{Ga} \rightarrow ^{66}\text{Zn}$	2019	$^{70}\text{As} \rightarrow ^{70}\text{Ge}$
381	$^{66}\text{Ge} \rightarrow ^{66}\text{Ga}$	1114	$^{70}\text{As} \rightarrow ^{70}\text{Ge}$	2189	$^{66}\text{Ga} \rightarrow ^{66}\text{Zn}$
426	$^{70}\text{Se} \rightarrow ^{70}\text{As}$	1120	$^{66}\text{Ge} \rightarrow ^{66}\text{Ga}$	2292	$^{66}\text{Ga} \rightarrow ^{66}\text{Zn}$
470	$^{66}\text{Ge} \rightarrow ^{66}\text{Ga}$	1232	$^{66}\text{Ga} \rightarrow ^{66}\text{Zn}$	2422	$^{66}\text{Ga} \rightarrow ^{66}\text{Zn}$
536	$^{66}\text{Ge} \rightarrow ^{66}\text{Ga}$	1333	$^{66}\text{Ga} \rightarrow ^{66}\text{Zn}$	2449	$^{70}\text{As} \rightarrow ^{70}\text{Ge}$
595	$^{70}\text{As} \rightarrow ^{70}\text{Ge}$	1338	$^{70}\text{As} \rightarrow ^{70}\text{Ge}$	2751	$^{66}\text{Ga} \rightarrow ^{66}\text{Zn}$
607	$^{70}\text{As} \rightarrow ^{70}\text{Ge}$	1356	$^{66}\text{Ga} \rightarrow ^{66}\text{Zn}$	2933	$^{66}\text{Ga} \rightarrow ^{66}\text{Zn}$
639	$^{66}\text{Ge} \rightarrow ^{66}\text{Ga}$	1387	$^{66}\text{Ga} \rightarrow ^{66}\text{Zn}$	3229	$^{66}\text{Ga} \rightarrow ^{66}\text{Zn}$
662	$^{66}\text{Ge} \rightarrow ^{66}\text{Ga}$	1411	$^{70}\text{As} \rightarrow ^{70}\text{Ge}$	3256	$^{66}\text{Ga} \rightarrow ^{66}\text{Zn}$
668	$^{70}\text{As} \rightarrow ^{70}\text{Ge}$	1418	$^{66}\text{Ga} \rightarrow ^{66}\text{Zn}$	3380	$^{66}\text{Ga} \rightarrow ^{66}\text{Zn}$
705	$^{66}\text{Ge} \rightarrow ^{66}\text{Ga}$	1460	$^{40}\text{K} \rightarrow ^{40}\text{Ar}$	3422	$^{66}\text{Ga} \rightarrow ^{66}\text{Zn}$
719	$^{66}\text{Ga} \rightarrow ^{66}\text{Zn}$	1495	$^{70}\text{As} \rightarrow ^{70}\text{Ge}$		

the curve in Figure 4.3. During the implantation at a rate  $R$ , the number of nuclei  $N$  grows as a function of time  $t$ , with the initial condition  $N(0) = 0$  as follows:

$$\frac{dN}{dt} = R - \lambda N(t), \quad (4.7a)$$

$$N(t) = \frac{R}{\lambda}(1 - e^{-\lambda t}), \quad (4.7b)$$

where  $\lambda$  is the decay constant equal to  $\ln(2)/t_{1/2}$ . The activity  $A$  is then defined as:

$$A(t) = \lambda N(t) = R(1 - e^{-\lambda t}). \quad (4.8)$$

After the beam delivery is stopped at  $t = t_{off}$ , the number of nuclei decays as:

$$dN = -\lambda N(t)dt, \quad (4.9a)$$

$$N(t) = N(t = t_{off})e^{-\lambda t}. \quad (4.9b)$$

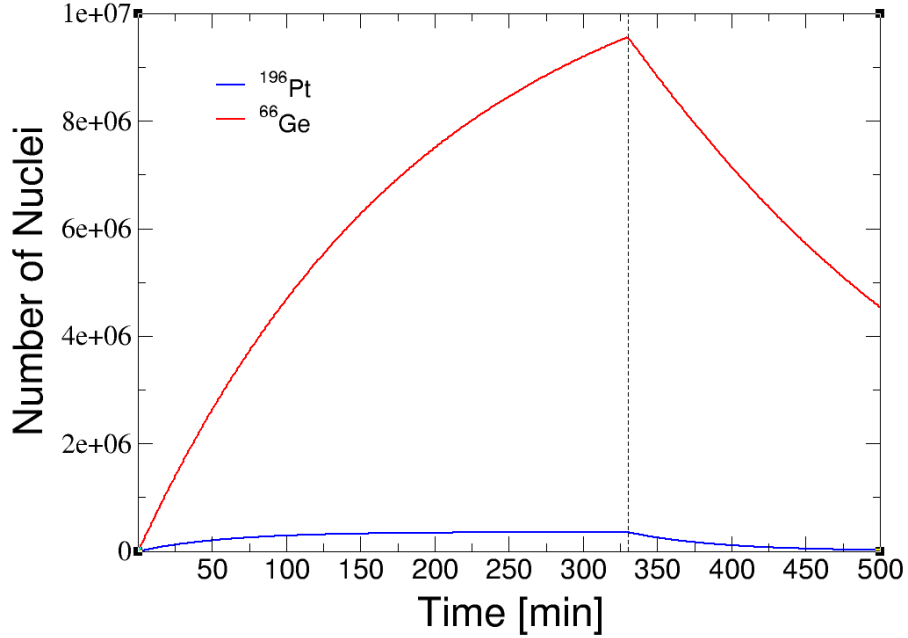


FIGURE 4.14: Number of nuclei as a function of time for  $^{66}\text{Ge}$  ( $t_{1/2} = 2.26$  h) and  $^{70}\text{Se}$  ( $t_{1/2} = 41$  min) for beam intensity  $R = 1000$  and  $N_{Ge}(t = 0) = N_{Se}(t = 0) = 0$ . The beam is on from  $t = 0$  to 330 min.

The duty factor is defined as the ratio of the number of nuclei delivered to the number of nuclei which have decayed as a function of time. From Equations 4.7b and 4.9b, the duty factors for the implantation and decay periods are given, respectively, by:

$$DF_{t_{on}} = \frac{N_{decay}}{N_{delivered}} = \frac{A(t)}{R} = 1 - e^{-\lambda t_{on}}, \quad (4.10)$$

$$DF_{t_{off}} = \frac{N_{decay}}{N_{delivered}} = \frac{N(t = t_{on}) - N(t)}{N(t = t_{on})} = 1 - e^{-\lambda t_{off}}. \quad (4.11)$$

The total duty factor is the sum of the duty factors for the implantation and decay periods, corrected for the decays during the implantation period:

$$DF = DF_{t_{on}} + (1 - DF_{t_{on}})DF_{t_{off}}. \quad (4.12)$$

The ratio of  $^{66}\text{Ge}$  to  $^{70}\text{Se}$  nuclei in the beam is then defined as:

$$\frac{f_{Ge}}{f_{Se}} = \frac{N_{\lambda,Ge}/DF_{Ge}}{N_{\lambda,Se}/DF_{Se}}. \quad (4.13)$$

From this ratio, the fraction of  $^{66}\text{Ge}$  in the beam can be extracted as:

$$f_{Ge} = 1 - \frac{1}{1 + (f_{Ge}/f_{Se})} = 0.89 \pm 0.12. \quad (4.14)$$

This number is in agreement with the  $^{66}\text{Ge}:^{70}\text{Se}$  ratio of 10:1 ( $\sim 90\%$ ) measured at the tape station at ISOLDE during the experiment.

## 4.5 Extracting Nuclear Structure Information

In CE experiments, the  $\gamma$ -ray intensities corresponding to the scattering of the collision partners is a direct observable. The matrix elements that couple these transitions is not a direct observable and occur as correlated parameters when fitting  $\gamma$ -ray intensity data. The integrated yields for the  $2_1^+ \rightarrow 0_1^+$  transitions in  $^{66}\text{Ge}$  and  $^{196}\text{Pt}$  were calculated using the semi-classical couple-channel Coulomb-excitation least-squares code GOSIA. The calculation was performed using known spectroscopic information such as level lifetimes, branching ratios and matrix elements. The GOSIA files used in the calculation is shown in Appendix A. The level scheme of  $^{66}\text{Ge}$  that was used to perform the GOSIA calculations is shown Figure 4.15 and the level scheme for  $^{196}\text{Pt}$  is shown in Figure 4.16.

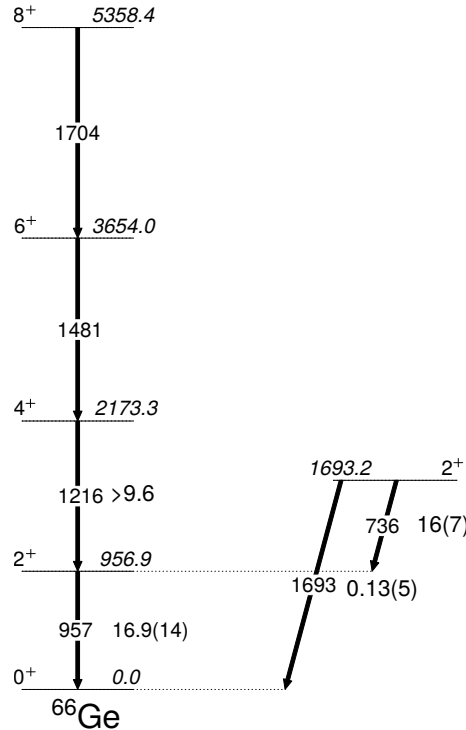


FIGURE 4.15: The level scheme used in the GOSIA calculations for  $^{66}\text{Ge}$  along with the known  $\gamma$ -ray energies and matrix elements.

The effects of higher-lying states in  $^{66}\text{Ge}$  were estimated using GOSIA by varying the  $\langle 2_1^+ || E2 || 2_2^+ \rangle$  matrix element and checking the percentage difference on the  $B(E2)$  and

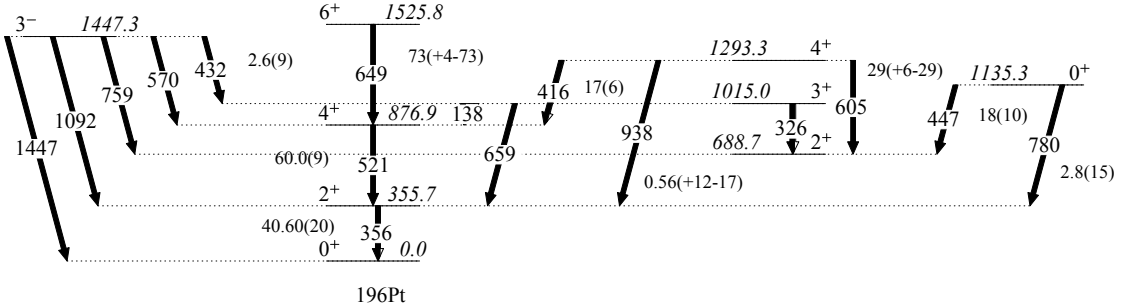


FIGURE 4.16: The level scheme used in the GOSIA calculations for  $^{196}\text{Pt}$  along with the known  $\gamma$ -ray energies and matrix elements.

$Q_s(2^+)$  value. The percentage difference was determined to be 1% and is considered in the error analysis. Figure 4.17 shows the experimental and theoretical beam gated heavy ion angular distributions integrated per 4 rings for the  $2_1^+ \rightarrow 0_1^+$  transition for  $^{66}\text{Ge}$  (left) and  $^{196}\text{Pt}$  (right). Figure 4.18 shows the experimental and theoretical target gated angular distributions integrated per 3 rings for the same transition.

The theoretical yields were calculated using  $\langle 0_1^+ || E2 || 2_1^+ \rangle = 0.4826$  eb and  $\langle 2_1^+ || E2 || 2_1^+ \rangle = 0.562$  eb, which were determined during this experiment. The theoretical yields were normalised to the experimental yields using a common normalization factor. As can be seen in the figures, the trend of the angular distribution produced by GOSIA is in agreement with the experimental yields.

The normalization procedure used in Ref. [30, 36] was applied to determine the  $\langle 2_1^+ || E2 || 2_2^+ \rangle$  matrix element. Coulomb excitation curves are determined in the  $\langle 2_1^+ || E2 || 2_2^+ \rangle - \langle 2_1^+ || E2 || 0_1^+ \rangle$  plane by fixing  $\langle 2_1^+ || E2 || 2_2^+ \rangle$  in steps of 0.01 eb, and varying  $\langle 2_1^+ || E2 || 0_1^+ \rangle$  until converging with the experimental intensity ratio between the target and the projectile. The intensity ratio is given by:

$$\frac{I_\gamma^T}{I_\gamma^P} = \frac{\sigma_{E2}^T W(\vartheta)^T}{\sigma_{E2}^P W(\vartheta)^P} = 0.915 \frac{N_\gamma^T \varepsilon_\gamma^P}{N_\gamma^P \varepsilon_\gamma^T} \quad (4.15)$$

where  $\varepsilon_\gamma^P$  and  $\varepsilon_\gamma^T$  are the relative efficiencies for the target and projectile respectively,  $W(\vartheta)$  is the integrated angular distribution of the de-excited  $\gamma$  rays in coincidence with the inelastic scattered particle, and the factor 0.915 accounts for the 97.25% enrichment of the  $^{196}\text{Pt}$  target chosen for normalization and the beam composition of 89% between  $^{66}\text{Ge}$  and  $^{70}\text{Se}$ . The normalization of the  $\gamma$  ray yields in  $^{66}\text{Ge}$  to the well known matrix elements in the target nucleus minimizes systematic effects such as dead time and pile up. Section 4.5.1 details how the  $B(E2)$  was extracted and section 4.5.2 discusses the determination of  $Q_s$ .

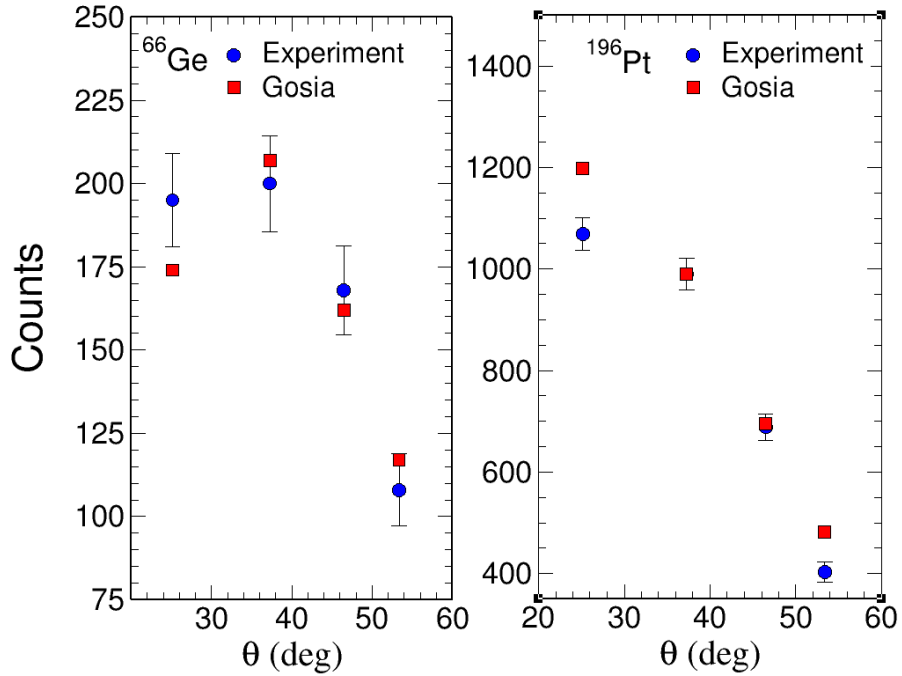


FIGURE 4.17: Beam gated heavy-ion angular distributions showing experimental and calculated  $\gamma$  ray yield integrated per 4 rings as a function of laboratory scattering angle,  $\theta$ , for the de-excitation of the  $2^+$  states in  $^{66}\text{Ge}$  (left) and  $^{196}\text{Pt}$  (right)

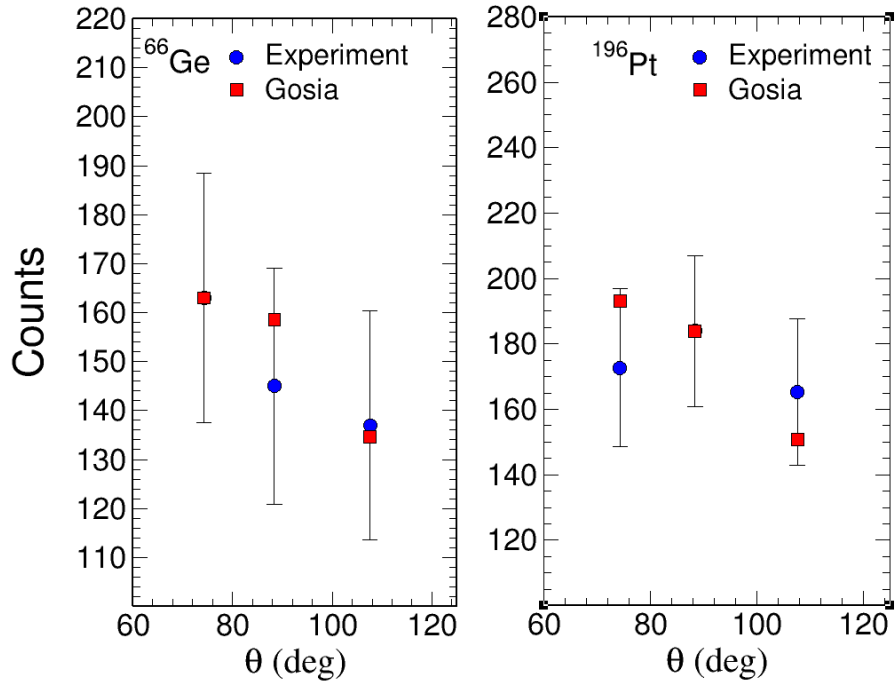


FIGURE 4.18: Target gated heavy-ion angular distributions showing experimental and calculated  $\gamma$  ray yield integrated per 3 rings as a function of laboratory scattering angle,  $\theta$ , for the de-excitation of the  $2^+$  states in  $^{66}\text{Ge}$  (left) and  $^{196}\text{Pt}$  (right)

### 4.5.1 Determination of $B(E2)$

The  $\langle 2_1^+ || E2 || 0_1^+ \rangle$  matrix element was determined using the beam gated data at forward angles [18.2° – 56.2°]. The angular range is safe from nuclear interaction contribution with a separation between nuclear surfaces of more than 5 fm as given by Cline's criterion.. Figure 4.19 shows the Coulomb cross section and excitation probability over the range of angles covered by the DSSSD in the laboratory frame.

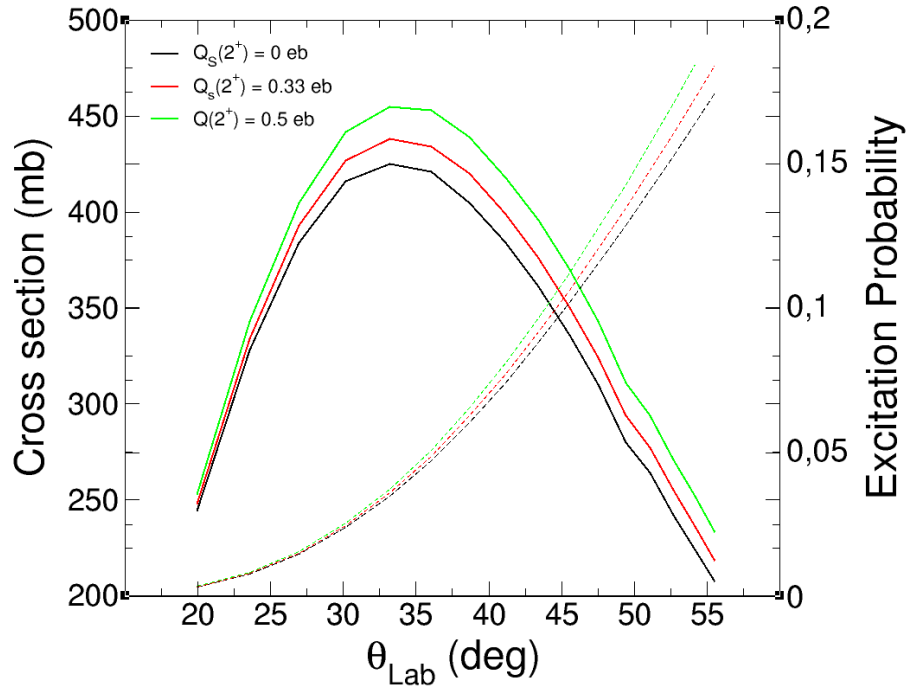


FIGURE 4.19: The coulomb cross section and excitation probability versus the labra-tory angles covered by the DSSSD. The cross section and excitation probability was calculated using GOSIA.

This range of angles is not sensitive to the quadrupole moment. The difference in  $Q_s(2^+)$  between 0.0 eb and 0.5 eb amounts to a 5% difference in the value of the  $B(E2)$  which was taken into account during the error analysis. Figure 4.20 depicts the beam gated non-doppler spectra from which the yields of the  $^{196}\text{Pt}$  were determined. Figure 4.21 shows the beam gated doppler corrected spectra from which the yields for the scattered  $^{66}\text{Ge}$  particles were determined.

The relative efficiencies,  $\varepsilon_\gamma^P = 733(50)$  and  $\varepsilon_\gamma^T = 1431(33)$ , and total counts of  $N_\gamma^P = 707(26)$  and  $N_\gamma^T = 3313(57)$  for the beam gated 355 and 956.9 keV transitions, yields an intensity ratio,  $\frac{I_\gamma^T}{I_\gamma^P} = 2.19(5)$ . A value of  $Q_s(2^+) = 0.33$  eb was calculated from the currently accepted  $B(E2; 2_1^+ \rightarrow 0_1^+) = 16.9(7)$  W.u. This yields a  $\langle 2_1^+ || E2 || 2_1^+ \rangle = 0.435$  eb, which was used in the GOSIA calculations. The  $\langle 2_1^+ || E2 || 2_1^+ \rangle$  matrix element was kept constant while incrementing  $\langle 2_1^+ || E2 || 0_1^+ \rangle$  in steps of 0.05 eb until the intensity

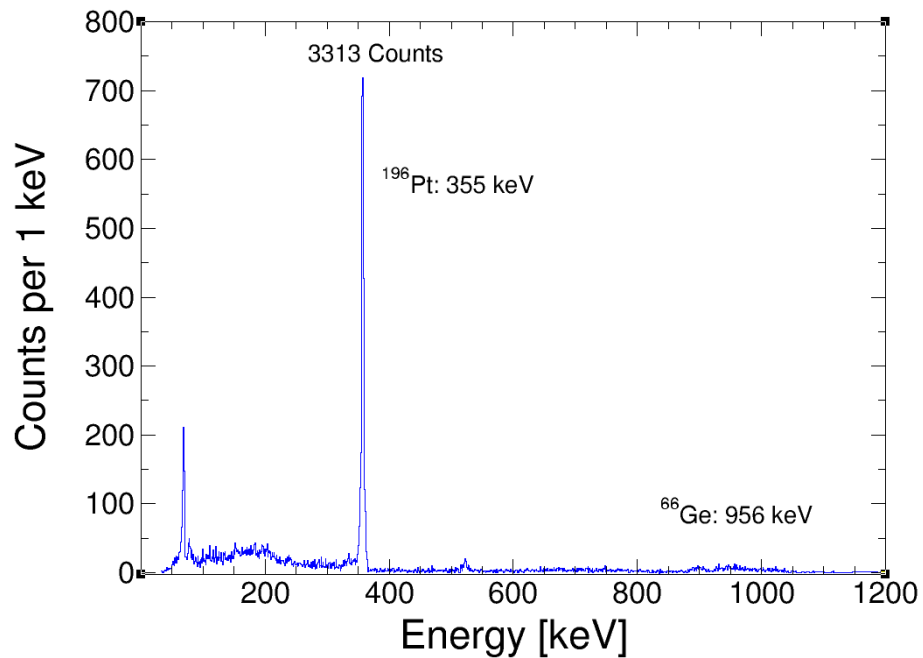


FIGURE 4.20: Beam gated non-Doppler spectra showing the number of counts for the 355 keV peak in  $^{196}\text{Pt}$ .

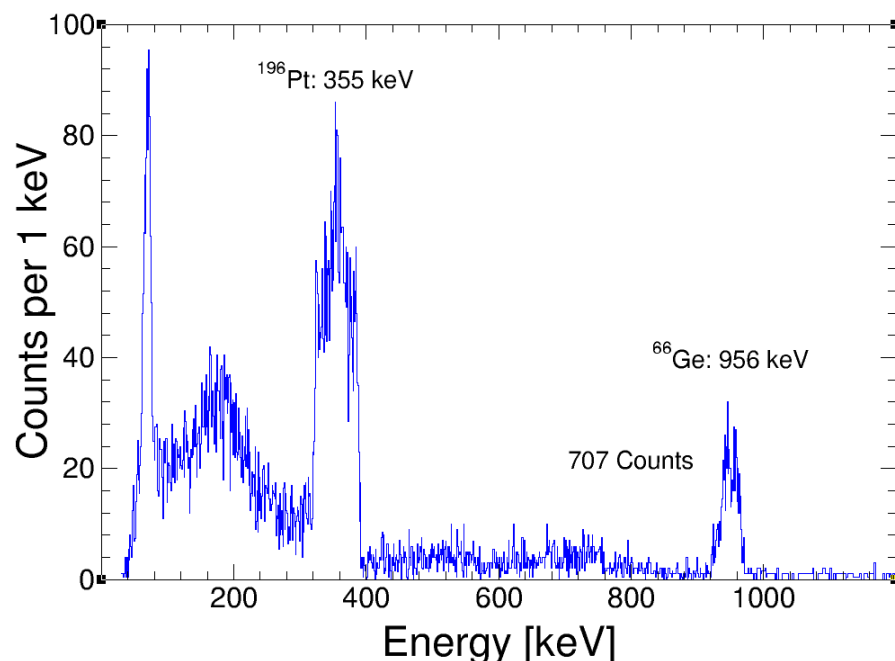


FIGURE 4.21: Beam gated Doppler corrected spectra showing the counts for the 956 keV peak in  $^{66}\text{Ge}$ .

ratio in Equation 4.15 converged. This yields a  $\langle 2_1^+ || E2 || 0_1^+ \rangle = 0.4826(15)$  eb giving a  $B(E2; 2_1^+ \rightarrow 0_1^+) = 29.4(20)$  W.u. The quoted error on this measurement comes from the  $1\sigma$  loci limits which is a 5% contribution, the quadrupole moments dependence on the  $B(E2; 2_1^+ \rightarrow 0_1^+)$  which is a 3% contribution, and the effects of higher-lying states on the  $B(E2; 2_1^+ \rightarrow 0_1^+)$  amounting to 1%, all added in quadrature.

#### 4.5.2 Determination of $Q_s$

The spectroscopic quadrupole moment  $Q_s(2^+)$  was determined using the target gated data in the recoiling angles. The angular range that covers the recoiling target was determined using the kinematics of the reaction. Figure 5.4 shows the scattered projectile angles vs the recoiling target angles for  $^{66}\text{Ge}$  bombarding a  $^{196}\text{Pt}$  target at 290.07 MeV.

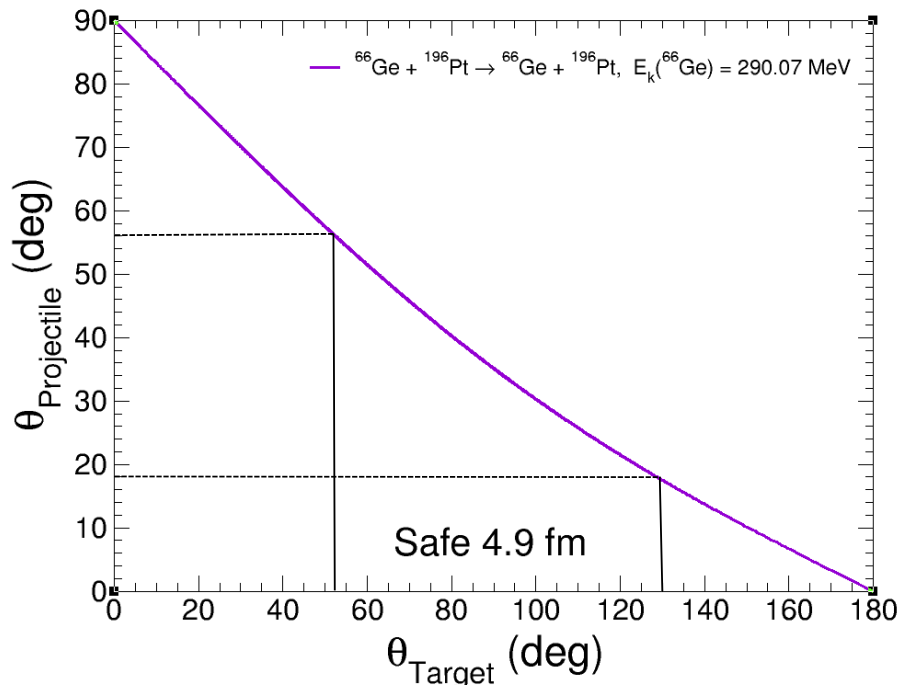


FIGURE 4.22: kinematics plot of target recoil angles vs particle scattering angles for  $^{66}\text{Ge}$  bombarding a  $^{196}\text{Pt}$  target at 290.07 MeV. The kinematics was calculated using LISE++.

The angular range of  $18.2^\circ - 56.2^\circ$  in the forward angles corresponds to an angular range of  $52.1^\circ - 128.1^\circ$  in the backwards angles. The separation of nuclear surfaces was checked using Cline's criterion up until  $128.1^\circ$  and was found to be not safe with a separation of nuclear surfaces of 4.81 fm. The first ring of the DSSSD, that corresponds to  $128.1^\circ - 119.5^\circ$ , was removed from the analysis resulting in Cline's criterion giving 4.92 fm separation between nuclear surfaces. Figure ?? shows the Coulomb cross section

and excitation probability versus the recoil angles covered by the DSSSD in the laboratory frame.

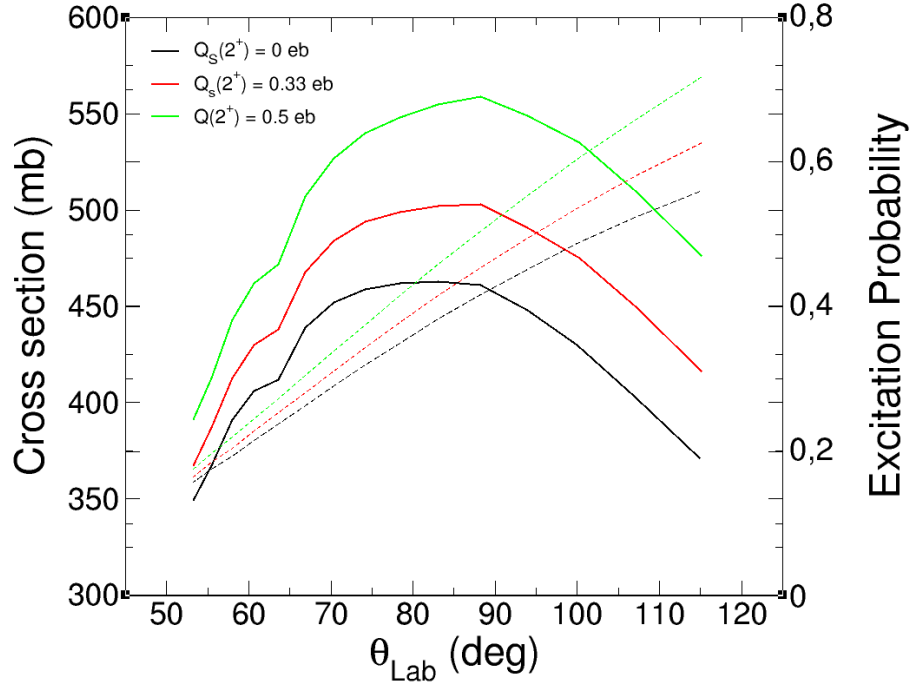


FIGURE 4.23: The coulomb cross section and excitation probability versus the recoil angles covered by the DSSSD. The cross section and excitation probability was calculated using GOSIA.

As can be seen from Figure 4.23, the last 6 rings of the DSSSD were not sensitive to  $Q_s(2^+)$  and was not used in the normalization, giving a final angular range of  $68.6^\circ - 119.1^\circ$ . The normalization technique described in Section 4.5 was used resulting in the Coulomb excitation diagonal band shown in Figure 4.24.

The dashed line represents the central value of the  $\langle 2_1^+ || E2 || 2_1^+ \rangle$  matrix element and the solid black lines represent the  $1\sigma$  loci limits. The horizontal band represents the  $B(E2; 2_1^+ \rightarrow 0_1^+) = 0.4827(15)$  determined during this experiment. A positive  $\langle 2_1^+ || E2 || 2_1^+ \rangle = 0.546(60)$  eb is obtained from the intersection of the two bands, corresponding to  $Q_s(2^+) = +0.41(0.4)$  eb. The error of  $\langle 2_1^+ || E2 || 2_1^+ \rangle$  is determined by the overlap region of the two bands assuming central values for the  $\langle 2_1^+ || E2 || 0_1^+ \rangle$ ,  $\pm 0.073$  eb, and the CE diagonal curve,  $\pm 0.096$  eb.

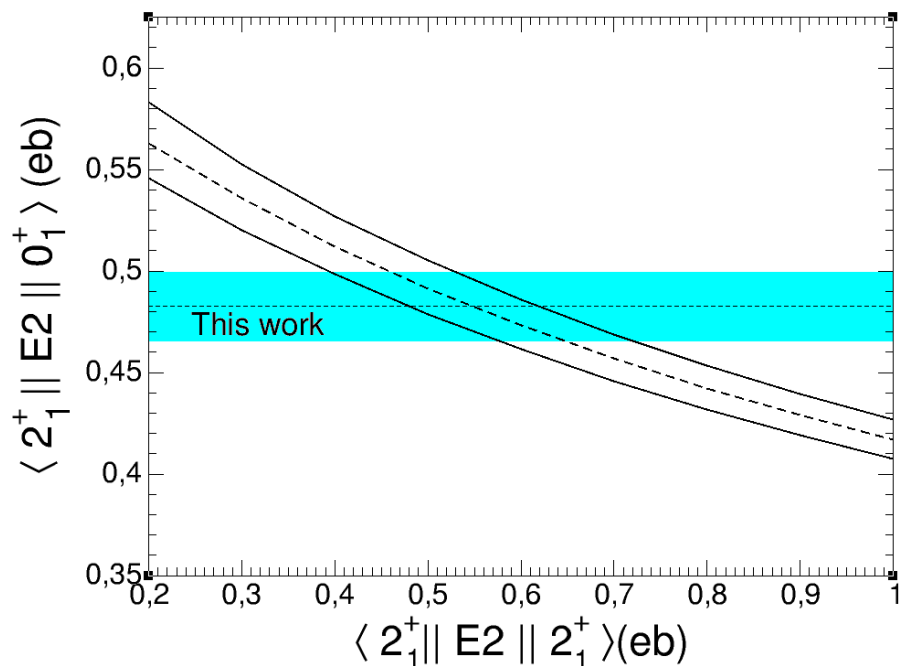


FIGURE 4.24: Variation of  $\langle 2_1^+ || E2 || 2_1^+ \rangle$  as a function of  $\langle 2_1^+ || E2 || 0_1^+ \rangle$  in  $^{66}\text{Ge}$ . The solid black lines represent the loci from the upper and lower limits of the intensity ratio. The horizontal band represents the  $1\sigma$  boundary for  $\langle 2_1^+ || E2 || 0_1^+ \rangle = 0.4827(15)$  eb.

## Chapter 5

# Results and Discussion

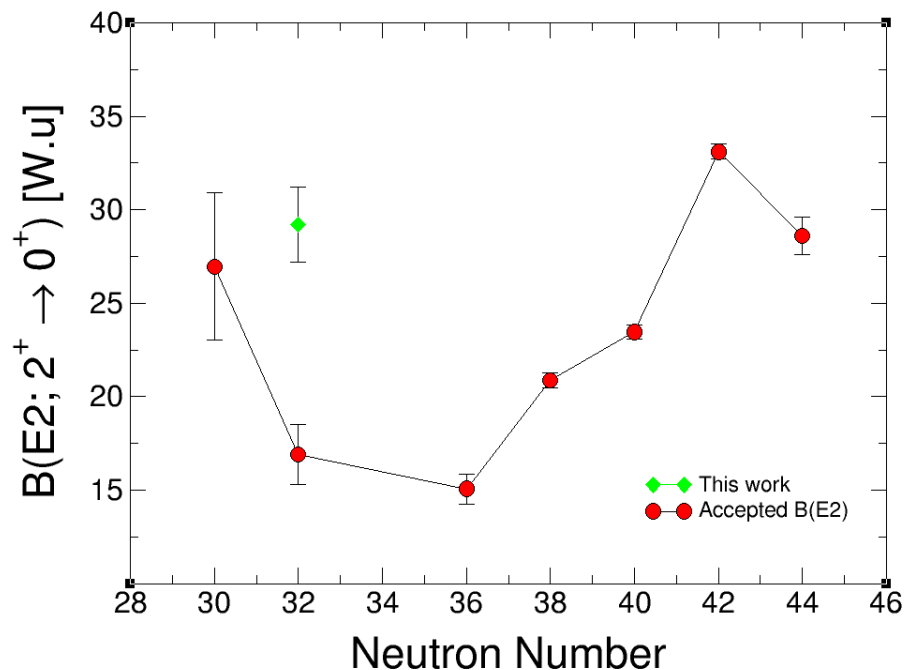


FIGURE 5.1: Adopted  $B(E2; 2^+_1 \rightarrow 0^+_1)$  values for even-even Ge isotopes. The  $B(E2; 2^+_1 \rightarrow 0^+_1)$  value determined during this experiment is shown in comparison.

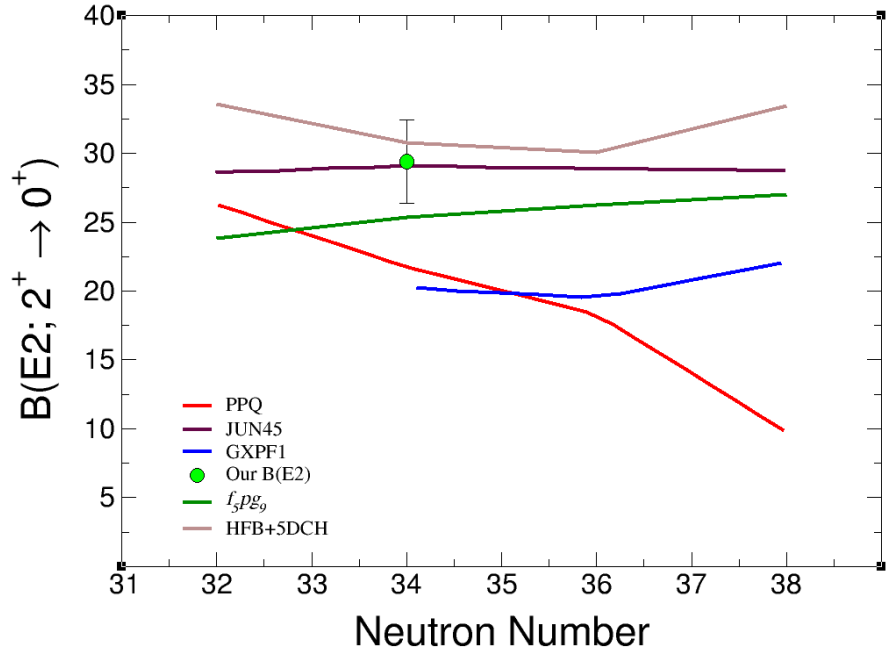


FIGURE 5.2: Adopted  $B(E2; 2_1^+ \rightarrow 0_1^+)$  values for even-even Ge isotopes. The  $B(E2; 2_1^+ \rightarrow 0_1^+)$  value determined during this experiment is shown in comparison.

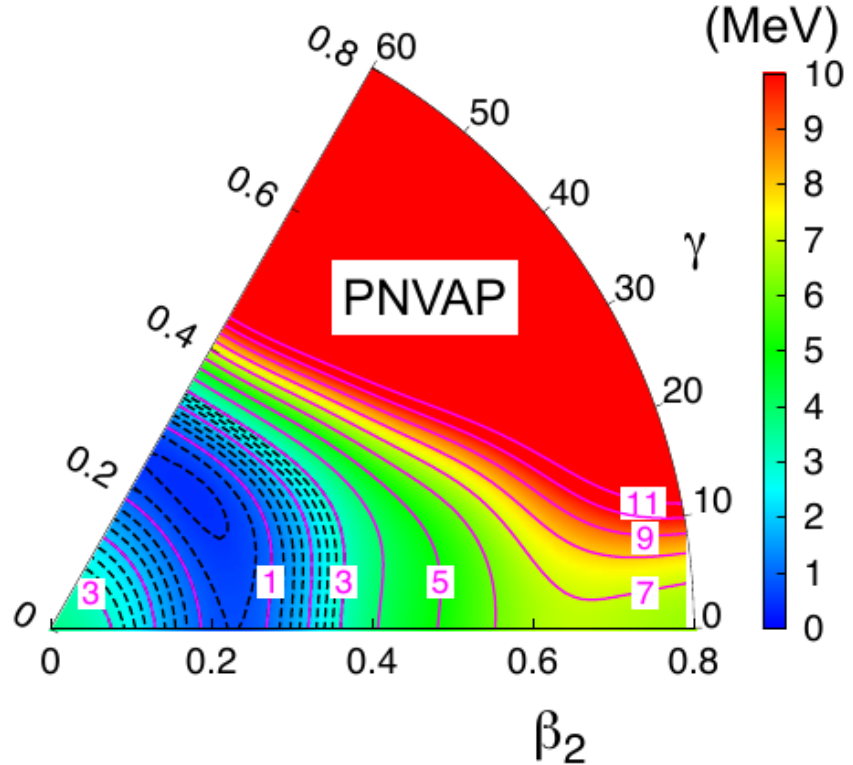


FIGURE 5.3: Adopted  $B(E2; 2_1^+ \rightarrow 0_1^+)$  values for even-even Ge isotopes. The  $B(E2; 2_1^+ \rightarrow 0_1^+)$  value determined during this experiment is shown in comparison.

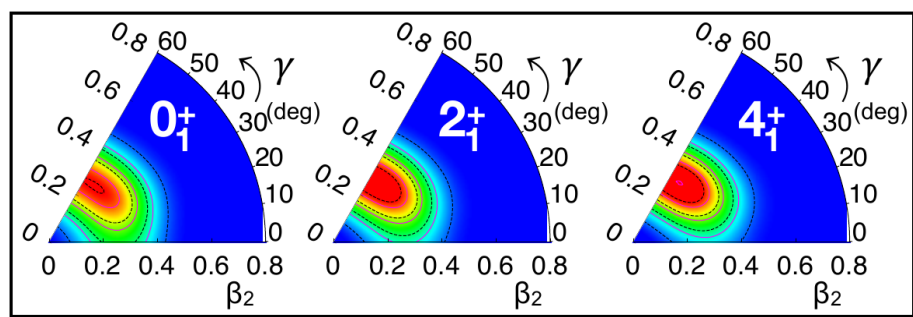


FIGURE 5.4: Adopted  $B(E2; 2_1^+ \rightarrow 0_1^+)$  values for even-even Ge isotopes. The  $B(E2; 2_1^+ \rightarrow 0_1^+)$  value determined during this experiment is shown in comparison.

## **Chapter 6**

# **Conclusion**

## **Appendix A**

### **Additional Test Results 1**

## **Appendix B**

## **Additional Test Results 2**

# Bibliography

- [1] K. Alder, A. Bohr, T. Huus, B. Mottelson, and A. Winther, “Study of nuclear structure by electromagnetic excitation with accelerated ions,” *Rev. Mod. Phys.*, vol. 28, pp. 432–542, 1956.
- [2] K. Alder and A. Winther, *Electromagnetic Excitation: Theory of Coulomb Excitation with heavy Ions*. New York: North-Holland, 1975.
- [3] D. Bazin, O. Tarasov, M. Lewitowics, and O. Sorlin, “The program lise: a simulation of fragment separators,” *Nuclear Instruments methods phys, Research section A: Accelerators, Spectrometers, Detectors and Associate Equipment*, vol. 482, pp. 307–327, 2002.
- [4] F. Becker, A. Petrovici, J. Iwanicki, N. Amzal, W. Korten, K. Hauschild, A. Hursotel, C. Theisen, P. Butler, R. Cunningham, T. Czosnyka, G. de France, J. Gerl, P. Greenlees, K. Helariutta, R.-D. Herzberg, P. Jones, R. Julin, S. Juutinen, H. Kankaanp, M. Muikku, P. Nieminen, O. Radu, P. Rahkila, and C. Schlegel, “Coulomb excitation of  $^{78}\text{Kr}$ ,” *Nuclear Physics A*, vol. 770, no. 3, pp. 107 – 125, 2006.
- [5] L. biedenharn and P. Brussaard, *Coulomb Excitation*. Oxford library of physical science: Clarendon Press, 1965.
- [6] A. Bohr and B. Mottelson, *Nuclear Structure II*. Reading: W.A. Benjamin, 1975.
- [7] M. Borge and K. Riisager, “Hie-isolde, the project and the physics opportunities,” *The European Physical Journal A*, vol. 52, 2016.
- [8] E. Bouchez, I. Matea, W. Korten, F. Becker, B. Blank, C. Borcea, A. Buta, A. Emsalem, G. de France, J. Genevey, F. Hannachi, K. Hauschild, A. Hürstel, Y. Le Coz, M. Lewitowicz, R. Lucas, F. Negoita, F. d. O. Santos, D. Pantelica, J. Pinson, P. Rahkila, M. Rejmund, M. Stanoiu, and C. Theisen, “New shape isomer in the self-conjugate nucleus  $^{72}\text{Kr}$ ,” *Phys. Rev. Lett.*, vol. 90, p. 082502, 2003.
- [9] R. Caten, *Nuclear Structure from a Simple Perspective*. New York Oxford: Oxford University Press, 1990.

- [10] P. Cejnar, J. Jolie, and R. Carsten, “Quantum phase transitions in the shapes of atomic nuclei,” *Rev. Mod. Phys.*, vol. 82, pp. 2155–2212, 2010.
- [11] N. N. D. Center, “Adopted b(e2) values,” Available at <https://www.nndc.bnl.gov/be2/adopted.jsp>.
- [12] N. N. D. Center, “National nuclear data center,” Available at <https://www.nndc.bnl.gov/>.
- [13] E. Clément, A. Görgen, W. Korten, E. Bouchez, A. Chatillon, J.-P. Delaroche, M. Girod, H. Goutte, A. Hürstel, Y. L. Coz, A. Obertelli, S. Péru, C. Theisen, J. N. Wilson, M. Zielińska, C. Andreoiu, F. Becker, P. A. Butler, J. M. Casandjian, W. N. Catford, T. Czosnyka, G. d. France, J. Gerl, R.-D. Herzberg, J. Iwanicki, D. G. Jenkins, G. D. Jones, P. J. Napiorkowski, G. Sletten, and C. N. Timis, “Shape coexistence in neutron-deficient krypton isotopes,” *Phys. Rev. C*, vol. 75, p. 054313, 2007.
- [14] D. Cline, “Nuclear shapes studied by coulomb excitation,” *Annual Review of Nuclear and Particle Science*, vol. 36, pp. 683–716, 1986.
- [15] D. Cline, T. Czosnyka, A. Hayes, P. Napiorkowski, N. Warr, and C. Wu, *GOSIA user manual for simulation and analysis of Coulomb excitation experiment*. GOSIA steering committee, 2012.
- [16] A. Corsi, J.-P. Delaroche, A. Obertelli, T. Baugher, D. Bazin, S. Boissinot, F. Flavigny, A. Gade, M. Girod, T. Glasmacher, G. F. Grinyer, W. Korten, J. Libert, J. Ljungvall, S. McDaniel, A. Ratkiewicz, A. Signoracci, R. Stroberg, B. Sulignano, and D. Weisshaar, “Collectivity of light ge and as isotopes,” *Phys. Rev. C*, vol. 88, p. 044311, 2013.
- [17] J. de Boer and J. Eichler, *The Reorientation Effect*. Boston, MA: Springer US, 1968, pp. 1–65.
- [18] A. de Shalit and M. Goldhaber, “Mixed configurations in nuclei,” *Phys. Rev.*, vol. 92, pp. 1211–1218, 1953.
- [19] H. Dejbakhsh, T. Cormier, X. Zhao, A. Ramayya, L. Chaturvedi, S. Zhu, J. Kormicki, J. Hamilton, M. Satteson, I. Lee, C. Baktash, F. McGowan, N. Johnson, J. Cole, and E. Zganjar, “Signature of the shape coexistence in  $^{72}\text{Kr}$ : discontinuities of the moment of inertia at low spin,” *Physics Letters B*, vol. 249, no. 2, pp. 195 – 199, 1990.
- [20] M. Girod, J.-P. Delaroche, A. Grgen, and A. Obertelli, “The role of triaxiality for the coexistence and evolution of shapes in light krypton isotopes,” *Physics Letters B*, vol. 676, no. 1, pp. 39–43, 2009.

- [21] M. Grieser, Y. Litvinov, R. Raabe, and e. a. K. Blaum, “Storage ring at hie-isolde,” *The European Physical Journal Special Topics*, vol. 207, pp. 1–117, 2012.
- [22] A. Gustafsson, A. Herlert, and F. Wenander, “Mass-selective operation with rex-trap,” *Nuclear Instruments methods phys, Research section A: Accelerators, Spectrometers, Detectors and Associate Equipment*, vol. 626, pp. 8–15, 2011.
- [23] D. Habs, O. Kester, T. Sieber, and et al., “The rex-isolde project,” *Hyperfine Interactions*, vol. 129, pp. 43–66, 2000.
- [24] K. Heyde and J. Wood, “Shape coexistence in atomic nuclei,” *Rev. Mod. Phys.*, vol. 83, pp. 1467–1521, 2011.
- [25] A. M. Hurst, P. A. Butler, D. G. Jenkins, P. Delahaye, F. Wenander, F. Ames, C. J. Barton, T. Behrens, A. Bürger, J. Cederkäll, E. Clément, T. Czosnyka, T. Davinson, G. de Angelis, J. Eberth, A. Ekström, S. Franchoo, G. Georgiev, A. Görgen, R.-D. Herzberg, M. Huyse, O. Ivanov, J. Iwanicki, G. D. Jones, P. Kent, U. Köster, T. Kröll, R. Krücken, A. C. Larsen, M. Nespolo, M. Pantea, E. S. Paul, M. Petri, H. Scheit, T. Sieber, S. Siem, J. F. Smith, A. Steer, I. Stefanescu, N. U. H. Syed, J. Van de Walle, P. Van Duppen, R. Wadsworth, N. Warr, D. Weisshaar, and M. Zielińska, “Measurement of the sign of the spectroscopic quadrupole moment for the  $2_1^+$  state in  $^{70}\text{Se}$ : No evidence for oblate shape,” *Phys. Rev. Lett.*, vol. 98, 2007.
- [26] Y. Kadi, Y. Blumenfeld, W. V. Delsolaro, M. A. Fraser, M. Huyse, A. P. Koufidou, J. A. Rodriguez, and F. Wenander, “Post-accelerated beams at ISOLDE,” *Journal of Physics G: Nuclear and Particle Physics*, vol. 44, no. 8, 2017.
- [27] A. Kavka, C. Fahlander, A. Bcklin, D. Cline, T. Czosnyka, R. Diamond, D. Disdier, W. Kernan, L. Kraus, I. Linck, N. Schulz, J. Srebrny, F. Stephens, L. Svensson, B. Varnestig, E. Vogt, and C. Wu, “Coulomb excitation of  $^{76,80,82}\text{Se}$ ,” *Nuclear Physics A*, vol. 593, no. 2, pp. 177–211, 1995.
- [28] E. Kugler, “The isolde facility,” *Hyperfine Interactions*, vol. 129, pp. 23–42, 2000.
- [29] E. Kugler, D. Fiander, B. Jonson, H. Haas, A. Przewloka, H. Ravn, D. Simon, and K. Zimmer, “The new cern-isolde on-line mass-seperator facility at the ps-booster,” *Nuclear Instruments and Methods in Physics Research B*, vol. 70, pp. 41–49, 1992.
- [30] M. Kumar Raju, J. Orce, P. Navrtil, G. Ball, T. Drake, S. Triambak, G. Hackman, C. Pearson, K. Abrahams, E. Akakpo, H. Al Falou, R. Churchman, D. Cross, M. Djongolov, N. Erasmus, P. Finlay, A. Garnsworthy, P. Garrett, D. Jenkins, R. Kshetri, K. Leach, S. Masango, D. Mavela, C. Mehl, M. Mokgolobotho, C. Ngwetsheni, G. O’Neill, E. Rand, S. Sjue, C. Sumithrarachchi, C. Svensson, E. Tardiff,

- S. Williams, and J. Wong, “Reorientation-effect measurement of the first  $2+$  state in  $^{12}\text{C}$ : Confirmation of oblate deformation,” *Physics Letters B*, vol. 777, pp. 250 – 254, 2018.
- [31] J. Ljungvall, A. Görzen, M. Girod, J.-P. Delaroche, A. Dewald, C. Dossat, E. Farnea, W. Korten, B. Melon, R. Menegazzo, A. Obertelli, R. Orlandi, P. Petkov, T. Pissulla, S. Siem, R. P. Singh, J. Srebrny, C. Theisen, C. A. Ur, J. J. Valiente-Dobón, K. O. Zell, and M. Zielińska, “Shape coexistence in light se isotopes: Evidence for oblate shapes,” *Phys. Rev. Lett.*, vol. 100, 2008.
- [32] R. Lutter, O. Schaile, K. Schoffel, K. Steinberger, P. Thirolf, and C. Broude, “Marjsubzaj/subzboou - a mbs and root based online/offline utility,” *Nuclear Science, IEEE Transactions on*, vol. 47, pp. 280–283, 2000.
- [33] R. Luttke *et al.*, “Collectivity in Ge-66 and Ge-68 via lifetime measurements,” *Phys. Rev. C*, vol. 85, p. 017301, 2012.
- [34] D. Moltz, J. Robertson, E. Norman, J. Burde, and C. Beausang, “Low-lying level structure of  $^{73}\text{Kr}$ ,” *Nuclear Physics A*, vol. 562, no. 1, pp. 111 – 120, 1993.
- [35] W. Nrenberg and H. Weidenmller, *Introduction to the Theory of Heavy-ion Collisions*. Berlin Heidelberg GmbH: Springer-Verlag, 1976.
- [36] J. N. Orce, T. E. Drake, M. K. Djongolov, P. Navrátil, S. Triambak, G. C. Ball, H. Al Falou, R. Churchman, D. S. Cross, P. Finlay, C. Forssén, A. B. Garnsworthy, P. E. Garrett, G. Hackman, A. B. Hayes, R. Kshetri, J. Lassen, K. G. Leach, R. Li, J. Meissner, C. J. Pearson, E. T. Rand, F. Sarazin, S. K. L. Sjue, M. A. Stoyer, C. S. Sumithrarachchi, C. E. Svensson, E. R. Tardiff, A. Teigelhoefer, S. J. Williams, J. Wong, and C. Y. Wu, “Reorientation-effect measurement of the  $\langle 2_1^+ \parallel E2 \parallel 2_1^+ \rangle$  matrix element in  $^{10}\text{Be}$ ,” *Phys. Rev. C*, vol. 86, p. 041303, 2012.
- [37] J. Ordan and CERN, “Isolde experiment july 2017,” <https://cds.cern.ch/record/2273290>, accessed: 2020-04-22.
- [38] A. Ostrowskia, S. Cherubinib, T. Davinsona, D. Groombridgea, A. Lairda, A. Musumarrab, A. Ninaneb, A. di Pietroa, A. Shotterea, and P. Woodsa, “Cd: A double sided silicon strip detector for radioactive nuclear beam experiments,” *Nuclear Instruments and Methods in Physics Research A*, vol. 480, pp. 448–455, 2002.
- [39] B. Pritychenko, M. Birch, B. Singh, and M. Horoi, “Tables of e2 transition probabilities from the first  $2+$  states in even-even nuclei,” *Atomic Data and Nuclear Data Tables*, vol. 107, pp. 1 – 139, 2016.

- [40] D. Radford, “Notes on the use of the program gf3,” Available at <https://radware.phy.ornl.gov/gf3/>.
- [41] K. Sato and N. Hinohara, “Shape mixing dynamics in the low-lying states of proton-rich kr isotopes,” *Nuclear Physics A*, vol. 849, no. 1, pp. 53–71, 2011.
- [42] M. Sugawara, Y. Toh, T. Czosnyka, M. Oshima, T. Hayakawa, H. Kusakari, Y. Hatsukawa, J.-i. Katakura, M. Matsuda, T. Morikawa, A. Seki, and F. Sakata, “Multiple coulomb excitation interpretation of the ge-70 beam and the interpretation of the o-2(+) as a deformed intruder,” *European Physical Journal A*, vol. 16, pp. 409–414, 01 2003.
- [43] Y. Tokunaga, H. Seyfarth, O. Schult, H. Brner, C. Hofmeyr, G. Barreau, R. Brissot, U. Kaup, and C. Mnkemeyer, “The 75se(n, )76se reaction and the low-lying level structure of 76se,” *Nuclear Physics A*, vol. 411, no. 2, pp. 209 – 230, 1983.
- [44] R. von Hahn, M. Grieser, D. Habs, E. Jaeschke, C. Kleffner, J. Liebmann, S. Papureanu, R. Repnow, D. Schwalm, and M. Stampfer, “Development of seven-gap resonators for the heidelberg high current injector,” *Nuclear Instruments methods phys, Research section A: Accelerators, Spectrometers, Detectors and Associate Equipment*, vol. 328, pp. 270–274, 1993.
- [45] R. Wadsworth, L. P. Ekstrom, G. D. Jones, F. Kearns, T. P. Morrison, O. M. Mustaffa, H. G. Price, P. J. Twin, and N. J. Ward, “A study of the neutron-deficient isotope66ge,” *Journal of Physics G: Nuclear Physics*, vol. 5, no. 12, pp. 1761–1774, dec 1979.
- [46] N. Warr, J. V. de Walle, and e. a. M. Albers, “The Miniball spectrometer,” *Eur. Phys. J.*, vol. A49, p. 40, 2013.
- [47] F. Wenander, B. Jonson, L. Liljeby, and G. Nyman, “REXEBIS the Electron Beam Ion Source for the REX-ISOLDE project,” CERN, Geneva, Tech. Rep. CERN-OPEN-2000-320, 1998. [Online]. Available: <https://cds.cern.ch/record/478399>
- [48] A. Winther and J. de Boer, “A computer program for multiple coulomb excitation,” *Perspectives in Physics*, vol. 19, pp. 303–374, 1966.
- [49] J. Ziegler, J. Biersack, and M. Ziegler, “Srim the stopping and range of ions in matter,” *Nuclear Instruments and Methods in Physics Research B*, vol. 268, pp. 1818–1823, 2010.